University of South-Eastern Norway
Faculty of Technology, Natural Sciences and Maritime Sciences

–

Master's Thesis

Study programme: Master of Science in Micro and Nano Systems Technology

Spring/Autumn 2023

Prabin Kharel

Photocatalytic degradation of biochar modified nano composites

Subtitle Enhancing environmental remediation through photocatalysis

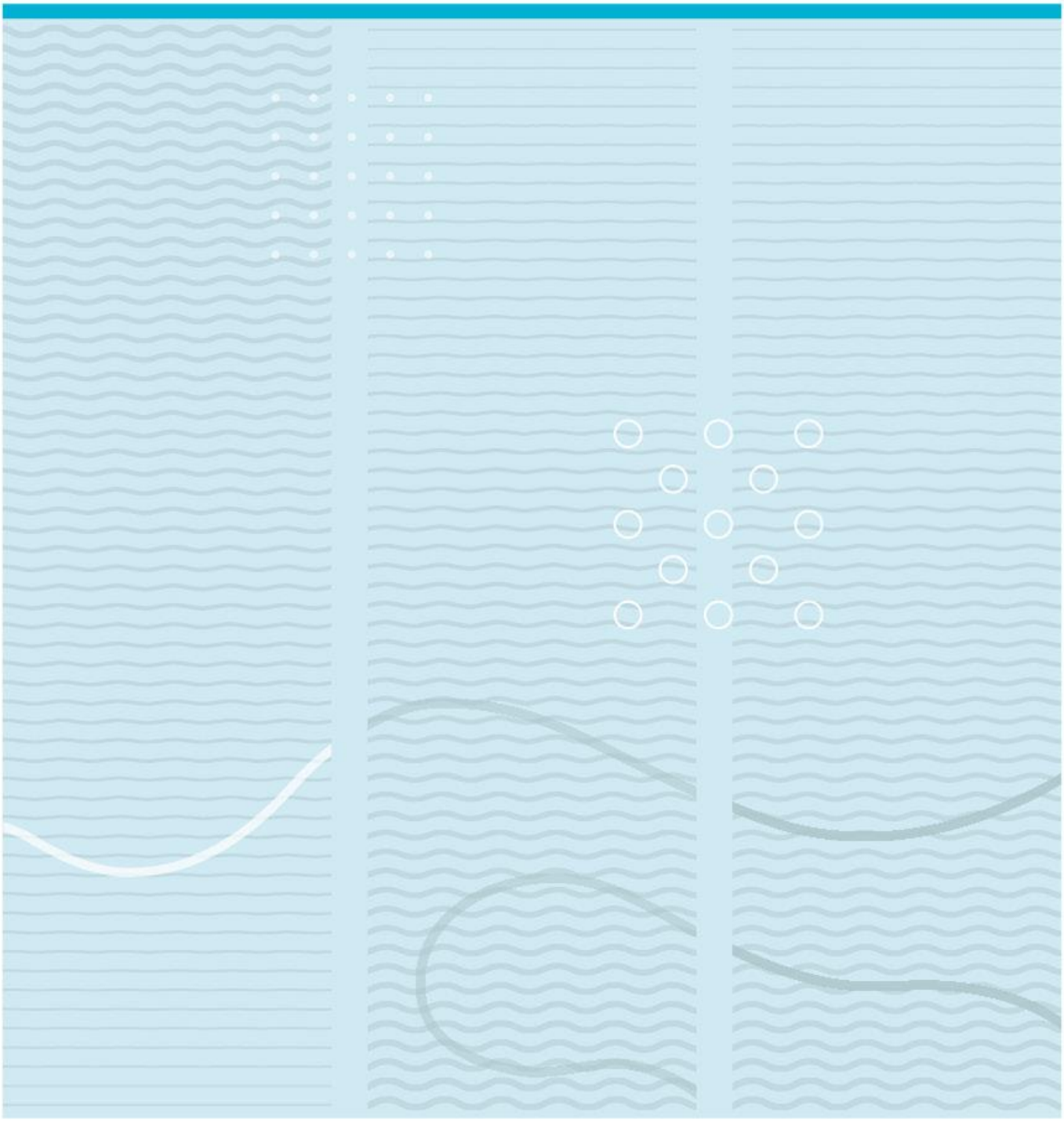

University of South-Eastern Norway
Faculty of Technology, Natural Sciences and Maritime Sciences
Department of Microsystems.
Raveien 215
NO-3184 Borre, Norway

http://www.usn.no

Summary

Contamination of surface water and groundwater from industrial discharges is a persistent environmental issue. In recent years, the development of solar photochemical approaches utilizing catalysts such as TiO_2, ZnO, and their composites has shown promising for oxidative degradation processes. In this study, we investigated the use of TiO_2, ZnO, and biochar composite catalysts for the photocatalytic degradation of methyl orange in wastewater. The catalysts were prepared using the autoclave method and characterized using XRD, SEM-EDS, FTIR, and UV-Vis spectrophotometry. The study also utilized a tungsten halogen light source (260 nm–2500 nm, 600 W) as one of the irradiation sources, which highlights the practicality of this approach. Our results showed that the addition of biochar to the catalysts enhanced their photocatalytic activity, with the TiO_2/biochar and ZnO/biochar composites displaying the highest efficiency, achieving a decolorization efficiency of up to 90%. The degradation process followed pseudo-first-order kinetics, with high r^2 values indicating a good fit. Our characterization results indicated that large surface area of biochar provides a higher contact area between the catalysts and pollutants, leading to more efficient adsorption and degradation. The utilization of TiO_2, ZnO, and biochar composite catalysts offers a practical solution for the efficient, cost-effective, and sustainable treatment of wastewater. Our study demonstrates the potential of these catalysts to remove various pollutants from wastewater, providing a constructive and eco-friendly perspective to water treatment. Lastly, this approach presents a sustainable and practical mitigation for the treatment of polluted water sources, offering benefits such as high efficiency and low environmental impact. Future studies can build upon these findings to develop more productive methods for water treatment.

Preface

I would like to extend my heartfelt appreciation to my supervisor, Professor Kaiying Wang, for his invaluable support throughout my journey. I would also like to express a special thanks to my co-supervisor, Dr. Osman Ürper, who played a crucial role in every aspect of my thesis, from sample preparation and characterization to the execution of various assays. Additionally, I would like to extend my gratitude to Dr. Marcela-Corina Roșu, a visiting research scientist from the National Institute for Research and Development of Isotopic and Molecular Technologies in Cluj-Napoca, Romania. Her presence and assistance have been invaluable to my research, and I am deeply appreciative of her help. Lastly, I would like to express my thanks to all the engineers at the USN lab for their constant and unwavering support, and I am truly grateful for their contributions.

<Horten/ 22/05/2023>

<Prabin Kharel>

Contents

.

1 Introduction

Planetary climate is changing at an accelerated rate and with greater intensity. Fossil fuel burning, deforestation, and land use have caused climate change since the mid-20th century. The impacts of climate change are wide ranging, including global warming, ocean level rise, and intense environmental events, which threaten food security, economic development, and human safety [1]. In addition, pollution levels are rising, intensifying the effects of climate change. Pollution has been identified as a significant source of concern for both human health and the environment. Unplanned Industrialization and urbanization have contributed to air and water pollution, causing substantial destruction and harm to ecosystems and human health. As an example, the synthetic dye methyl orange, widely used in industries and factories, has been identified as a pollutant which can degrade the quality of air and water if proper treatment is not done before it can be discharged [2]. Environmentalist suggested diverse techniques for removing toxic organic and inorganic compounds. However, the procedures are unproductive in terms of cost, efficiency, and the degradation of whole pollutants [3]. Among the diverse procedure and approach, photocatalysis is very imperative approach to remove toxic and harmful waste material like organic compounds [4]. It is one of the most promising methods which serves as a leading technique that removes all the pollutants under adequate temperature and pressure without initiating any secondary pollution. In this process, oxidation and hydrolysis work together to break down contaminants into safe organic compounds like H_2O and CO_2 [3], [4] and sun irradiation supplies enough energy to power this process. This method allows for the fragmentation of organic contaminants into smaller, and less harmful parts. Photocatalytic degradation is a key method for combating environmental pollution because of its sustainability, efficiency, versatility, cost-effectiveness, and health advantages.

This method is significant because it provides an environmentally viable method for eliminating contaminants from the air, water, and soil, which can help protect both human health and the environment. Furthermore, the intensity and wavelength of the light employed, the photocatalyst used, and the pollutant to be treated all have an impact on the process's success. Metal oxides, semiconductors, and carbon-based materials are only a few of the photocatalysts that have been developed for this purpose. Researchers are always working to improve the effectiveness and sustainability of photocatalytic degradation technologies to

address the growing issue of environmental pollution. Realizing the significance of photocatalysis, new prospects for designing and creating highly effective TiO_2, ZnO for various applications may arise for the removal of pollutants in upcoming years.

1.1 Motivation

This approach holds great potential because of the beneficial effect of photocatalytic degradation of organic pollutants over their transformation under ambient settings. A significant advantage of photocatalytic degradation is that solar energy is used for decontamination. Degradation of pollutants by photocatalysis depends heavily on many factors, including the pH of the solution, concentration of pollutant, volume of photocatalyst particles, shape, temperature, heat, the intensity of light, as well as availability of electron acceptors. It is possible to improve the mechanism of pollutant photodegradation by analyzing how these characteristics affect the photocatalytic properties of semiconductors, such as TiO_2 and ZnO. Consequently, photocatalysis can help reduce greenhouse gas emissions while reducing our dependence on fossil fuels. Photodegradation researchers may be motivated to learn how photocatalysis can improve this process to produce hydrogen more efficiently and sustainably.

Similarly, photodegradation can be used in various sectors, including wastewater treatment, industrial processes, air purification, and chemical and fuel production. Researchers can develop more scientific and systematic methods for photodegradation in these applications by better understanding the mechanisms involved. Similarly, photodegradation research can help researchers to learn more about the fundamental core of chemistry, biology, and physics and how these disciplines intersect in practice. Overall, the ability to decontaminate pollutants, create a clean environment, and safe human health makes photocatalytic degradation a vital area of research, with the potential to significantly impact environmental and industrial processes.

1.2 Objective of thesis

This research aims to analyze the photocatalytic breakdown of methyl orange linked to ZnO and TiO_2 photocatalyst and their mixtures with biochar. The performance of the photocatalyst will be evaluated using characterization techniques, including X-ray diffraction (XRD), Scanning electron microscopy-Energy dispersive spectroscopy (SEM-EDS), Fourier transform infrared spectroscopy (FTIR) and UV-visible spectrophotometry (UV-Vis). Through this study, we will gain a deeper understanding of the mechanisms behind photocatalytic degradation and the potential of these materials to remove harmful organic pollutants from water.

1.3 Outline view

The first chapter introduces the reader to photocatalytic degradation and emphasizes the importance of developing effective and sustainable technologies for this purpose. Additionally, it explores the project's motivation, goals, and thesis organization.

An overview of background of photocatalysis, history, various photocatalyst that have been studied, including TiO_2, ZnO, and biochar, and various synthesis techniques is specified in chapter 2.

The materials used in the study are described in chapter 3, including the starting materials for photocatalyst synthesis, the dyes and organic pollutants used for testing, and the characterization tools such as XRD, SEM-EDS, FTIR and UV-visible spectrophotometry. It describes the photocatalyst synthesis procedures using the hydrothermal method and sol-gel techniques, as well as the experimental setup and procedures used for photocatalytic degradation experiments, including the determination of optimal conditions and degradation mechanisms. Chapter 4 discusses the results obtained through diverse characterization tools.

Chapter 5, and chapter 6 discuss the conclusion of this study and suggest directions for future research on this topic.

2 Background and Literature Review

A chemical and physical characteristic of a material can be changed by exposure to light through photodegradation. The material may degrade due to this process, changing the material's color, tensile strength, and other characteristics. The methods of photo-oxidation, photo-hydrolysis, and photo-polymerization are just a few examples of the many ways that materials can degrade under the influence of light. Different elements can affect these pathways, including as the type of light exposure, the material's characteristics, and the presence of catalysts or other agents. Research on photodegradation has been conducted on various materials, including polymers, coatings, and pigments. However, further research is needed to understand the underlying mechanisms of photodegradation on various photocatalyst and to develop more effective strategies for preventing or mitigating its effects.

Research interest in using TiO_2 to decompose cyanide in water has grown since Frank and Bard investigated its potential in 1977 [5]. Last decades, attention has been focused broadly on the potential application of TiO_2 nanostructures as efficient photocatalysts in the degradation of a variety of organic contaminants into non-hazardous, non-toxic byproducts when exposed to UV or visible light. For instances, there is complete report on photo degradation of RhB dye over TiO_2 bilayer films under the wavelength of 365nm in 2010 [6]. Similarly, there has a been studied on the photo degradation of amino acid over TiO_2 in 2011 [7]. TiO_2 has a variety of uses worldwide, including the photocatalytic breakdown of organic pollutants in environmental purification processes, the photoelectrochemical splitting of water to produce hydrogen gas, the pollution of carbonic acid gases, and dye-sensitized solar cells. Due to its low cost, chemical inertness, and high photoefficiency, TiO_2 is the most often used material in heterogeneous photocatalysis. The ineffective utilization of visible light, limited adsorption capacity for hydrophobic pollutants, homogeneous dispersion in aqueous suspension, and post-recovery of the TiO_2 particles after water treatment are the critical technical commercialization[8]. Further improving the visible-light spectral sensitivity of TiO_2 is one of the key challenges faced by the community involved in the research of photocatalysis [9]. Thus, numerous studies have been conducted to use transition metals or non-metal components to expand the photocatalytic activity of titania into the visible light regime [10],[11]. ZnO, while on the other hand, has been successfully operated in a variety of applications, including gas sensor [12] ,

field effect transistors [13], Ultraviolet lasing behaviors [14], microcavity and efficient UV-visible optoelectronic devices [14], and light emitting diodes [15]. On comparisons with TiO_2, ZnO possess similar band gap 3.37 ev [16]. Nevertheless, it has diversified application including low cost, less toxic, low electronic noise and it can withstand higher electric fields. This quality of ZnO have truly witness the eye of worldwide analyst researcher for the utilize of it. Currently, titanium dioxide (TiO_2) or zinc oxide (ZnO) are often added to biochar to enhance its photodegradation capabilities. Biochar is a highly aromatic, carbon-rich solid material produced by low-cost and relatively low-temperature pyrolysis from a renewable resource or waste materials like wood chips, rice straw, dried leaves, etc. [19] and combing with ZnO and TiO_2 when exposed to light, they can effectively decompose organic material. There is still much to learn about the efficiency and possible uses of TiO_2-modified biochar and ZnO-modified biochar in photodegradation processes, which is why research is still being done in this area. But using photocatalysts like TiO_2 and ZnO in biochar has demonstrated potential as a method. Due to the biochar's huge specific surface area, alkalinity, abundance of functional groups, and ease of surface modification, TiO_2 or ZnO could be attached to it effectively. In the process of removing methyl orange from water resources, hybrid compounds comprised of titanium dioxide and biochar have also found use. According to research, using a combination of TiO_2 and biochar may remove up to more than 90% of methyl orange pollutant through photocatalysis when exposed to UV-visible light[17]. Another study conducted by Mayara Gabriela Gonçalves et al showed that the zinc oxide Biochar Modified Nanocomposites (ZnOMBNC) also demonstrated outstanding removal capabilities, with a maximum removal efficiency of around 90%[18].

2.1 Principle of heterogeneous photocatalysis

As we know, homogeneous catalysis entails a reaction where the catalyst and reactants are in the same phase. On the other hand, heterogeneous catalysis involves a process where catalyst and reactants are in distinct phases. Heterogeneous reactions have various advantages, including broad applicability, cost-effectiveness, and easy catalyst separation. Regardless of numerous photocatalysts, photocatalysis processes can be classified into five crucial phases, including Light absorption or harvesting, excitation and charge generation, charge separation-

transfer-migration, charge recombination or oxidation-reduction processes, and desorption of reaction products from the catalyst surface or reaction medium[19],[20]. The photocatalytic process is depicted in figure 2.1.

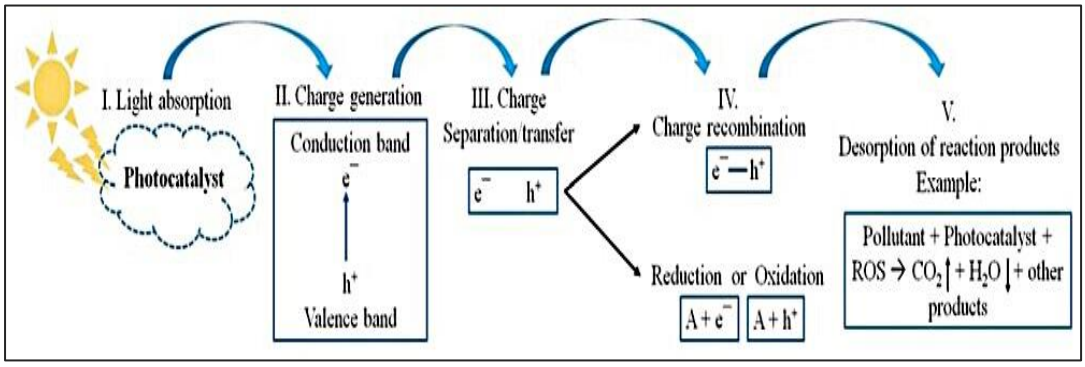

Figure 2.1: Steps wise photocatalysis mechanism illustration [20].

Photocatalysis is initiated by photo absorption by a catalyst. When incoming photon energy (E = *hv*) is equal to or greater than the band gap of photocatalyst (ΔE) where *v* is the frequency of incident light, and h is the Planck constant, then there will be photoexcitation of electrons from the valence band (VB) to conduction band (CB) (see figure 2.2), leaving a hole (h+) in the valence band edge by exciting an electron (e^-) to the conduction band edge (Eq.(1.1)). Due to the generation of a positive hole and electron, the oxidation-reduction reaction takes place at the surface of the semiconductor. In an oxidation reaction, the positive hole reacts with moisture on the surface producing hydroxyl radical $OH^{\cdot}$ (Eq. (1.2). Also, positive holes combine with hydroxyl ions, OH^- to form hydroxyl free radical $OH^{\cdot}$ (Eq. (1.3)). However, the free electrons present on the conduction band combined with atmospheric oxygen, producing superoxide radicals (O_2^-) (Eq. (1.4)) or hydrogen peroxides (H_2O_2) (Eq. (1.5)). Consequently, hydrogen peroxide dissociates into hydroxyl radical and hydroxyl ion (Eq. (1.6)). The hydroxyl radical generated is very oxidative and plays a significant role on the partial or complete decomposition of many organic compounds [21].

$$(TiO_2/ZnO) + h\nu \rightarrow e^- + h^+ \quad (1.1)$$

$$h^+ + H_2O \rightarrow H^+ + OH^{\cdot} \quad (1.2)$$

$$h^+ + OH^- \rightarrow OH^{\cdot} \quad (1.3)$$

$$e^- + O_2 \rightarrow O_2^- \quad (1.4)$$

$$2\,e^- + O_2 + 2\,H^+ \rightarrow H_2O_2 \quad (1.5)$$

$$e^- + H_2O_2 \rightarrow OH^{\cdot} + OH^- \quad (1.6)$$

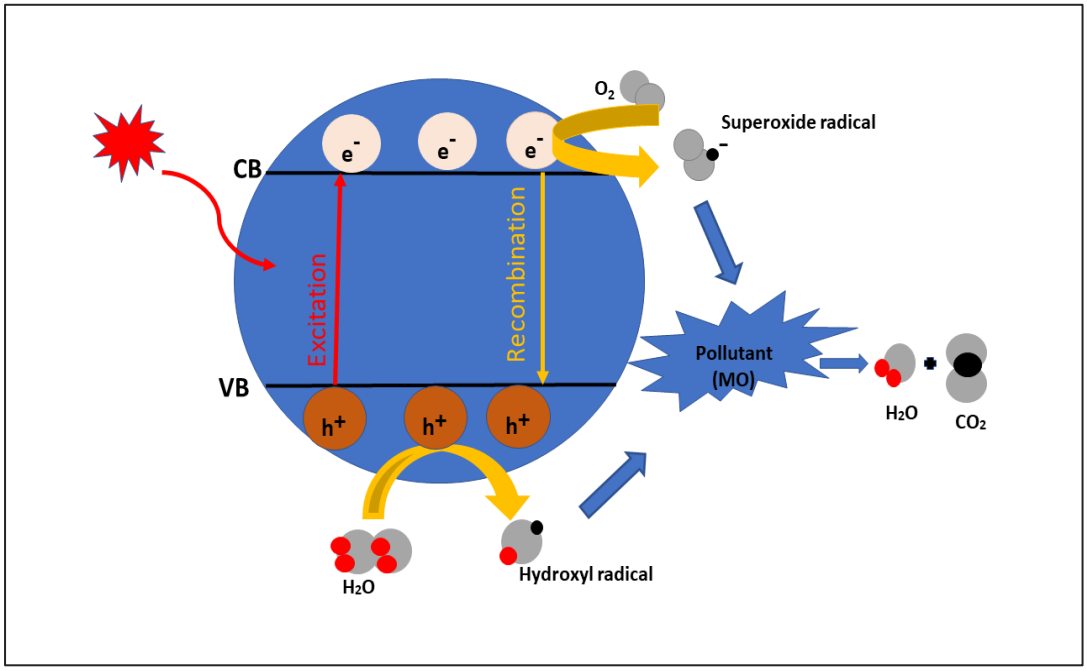

Figure 2.2:Schematic diagram of photocatalytic mechanism for TiO_2 / ZnO.

2.2 Types of Heterogeneous Photocatalyst

A heterogeneous photocatalyst is a catalyst that increases chemical reactions when light is present. Typically solid, these substances break down pollutants, produce hydrogen fuel, and synthesize chemicals and fuels from renewable sources. Most heterogeneous photocatalysis are formed from metal oxides, semiconductors, organic molecules, or enzymes. They function by absorbing light energy and utilizing it to start chemical processes on their surface.

2.2.1 Semi-conductor based photocatalyst.

In recent decades, Semiconductors such as TiO_2, ZnO, CdS, and SnO_2, have been used in photocatalysis due to their durability, low cost, low toxicity, super-hydrophilicity, and remarkable chemical and photochemical stability [22]. The Band gap energy is fundamental in the photocatalytic process. The band gap energies and band edge sites of typical semiconductor photocatalysts are shown in figure 2.3.

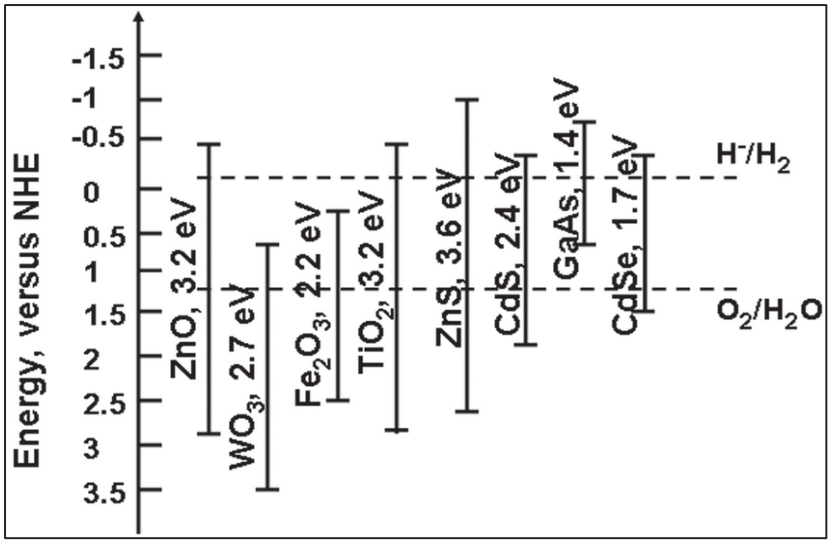

Figure 2.3: Band edge positions of common semiconductor photocatalysts[23],[24]

The band gap energy is one of the critical parameters that influence photocatalysis. Therefore, altering the band gap of the catalyst is one of the practical approaches to achieve the efficiency and productivity of photocatalysis, which can be done by mixing metal oxides, adding dopants, and changing particle shape on semiconductor [25]. Table 2.1 shows the values of the band gap energies of several semiconductors photocatalysts.

Table 2.1:Values of band bap energies of various semiconductor photocatalysts from DS Bhatkhande [26]

Photocatalyst	Band gap Energy (ev)	Photocatalyst	Band gap Energy (ev)
Si	1.1	ZnO	3.2
TiO_2 rutile	3.0	TiO_2 anatase	3.2
WO_3	2.7	CdS	2.4
ZnS	3.7	$SrTiO_3$	3.4
SnO_2	3.5	WSe_2	1.2
Fe_2O_3	2.2	α-Fe_2O_3	3.1

2.2.2 Noble and metal oxide based photocatalyst

Various noble metals (Ru, Pt, Rh, Ir, and Pd) and some metal oxides (Cu, Mn, Co, Cr, Ti, Bi, and Zn) have traditionally been used as heterogeneous catalysts [27]. It has been found that metal oxides like ZnO and TiO_2 are safer than other substances because they are less toxic. In

addition, combining two metal oxide catalysts may also enhanced non-selectivity and catalytic activity. Supporting noble metal on metal oxide surfaces has been reported to improve the activity and stability of the catalyst[28].

2.3 Titanium oxide based photocatalyst

Titanium dioxide (TiO_2) has been widely used as a photocatalyst in many environmental and energy applications due to its efficient photoactivity, high stability, low- cost, and safety to the environment and humans. However, it has poor affinity for hydrophobic organic pollutants [29]. Therefore, numerous procedures must be employed to eliminate the band gap energy and electron-hole recombination rate, as well as enhance the absorption of organic contaminants. This section overviews the common crystal structures of TiO_2 and its photocatalytic performance.

2.3.1 Crystal structure and morphology of TiO_2

Titanium dioxide (TiO_2), known as titania, can exist in either crystalline or amorphous forms. However, most TiO_2 can be found in three main crystalline polymorphs: anatase, rutile, and brookite. The anatase and rutile polymorphs have tetragonal structures, while brookite has an orthorhombic form [30]. Figure 2.4 depicts the crystal structures of these polymorphs, notably rutile, anatase, and brookite. It is critical to note that the different crystal forms of TiO_2 have the potential to alter its photocatalytic capabilities. These polymorphs have multiple characteristics and, thus, varying photocatalytic activity. The brookite phase, with its features and future applications, is still under investigation [30]. However, it has received far less attention than other phases of TiO_2. This is due primarily to the difficulty in generating pure brookite particles.

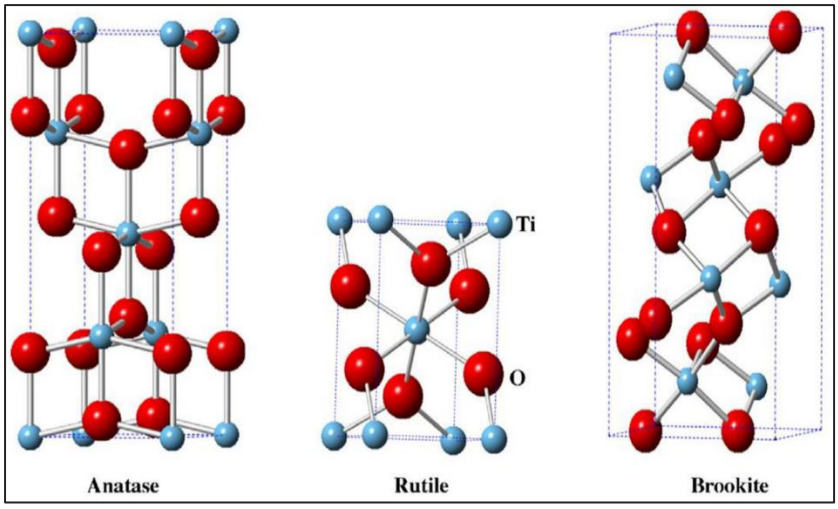

Figure 2.4: Crystal structure of anatase, rutile and brookite [31]

Anatase is thought to be the most photoactive phase for both antibacterial coatings and degradation of organic pollutants because of the low recombination rate of the photogenerated charge carriers and the high surface adsorptive potential towards the organic compounds[32]. Rutile is the stable phase, while anatase and brookite are metastable [33]. Table 2.2 offers a detailed analysis of the three phases, providing valuable insights into their characteristics and properties. This information can aid in understanding the behavior and performance of the phases in various applications.

Table 2.2:Crystallographic and Optical Properties of Titanium Dioxide Polymorphs [34]

Crystal Structure	Crystal Lattice	Lattice constant (A°).	RI	Band gap (ev)	Bulk conductivity (S cm^{-1})	Density (g/cm^{-3})
Rutile	Tetragonal	a =4.59 c=2.96	2.605–2.616, 2.890–2.903	3.0 ± 0.1	10^{-2} -10^{-7}	4.13
Anatase	Tetragonal	a =3.79 c= 9.51	2.561, 2.488	3.2 ± 0.1	5×10^{-8}	3.79
Brookite	Orthorhombic	a=9.17 b=5.46 c=5.14	2.583, 2.700	3.4± 0.1	3×10^{-7}	3.99

2.4 Zinc oxide photocatalyst

ZnO is a white powder used in plastics, glass, cement, rubber, and lubricants[35]. It is also an excellent electrical conductor with a wide bandgap, making it suitable for photonic and opto-electronic applications [36]. In addition to its industrial applications, ZnO is being studied for its potential photocatalytic properties. Upon exposure to light, the material undergoes a reaction where it produces both electrons and holes. These electrons and holes then react with oxygen and water, which leads to the creation of superoxide ions and hydroxyl radicals. Because these highly reactive species can decompose a wide range of organic compounds and pollutants, ZnO is a potential material for air and water purification.

2.4.1 Crystal structure of zinc oxide

As an II-VI semiconductor material with comprehensive band gap energy of 3.34 eV and considerable exciting binding energy (60 mv) at room temperature, ZnO is a potential material for optoelectronic applications [37],[38]. Over the past two decades, ZnO nanostructures have been investigated theoretically and experimentally and scientists and engineers believe that the specific shape of ZnO nanostructures has numerous applications[39]. Generally, zinc oxide crystallizes in different forms, including rocksalt, zinc blende and wurtzite structure as can be seen from Figure 2.5.

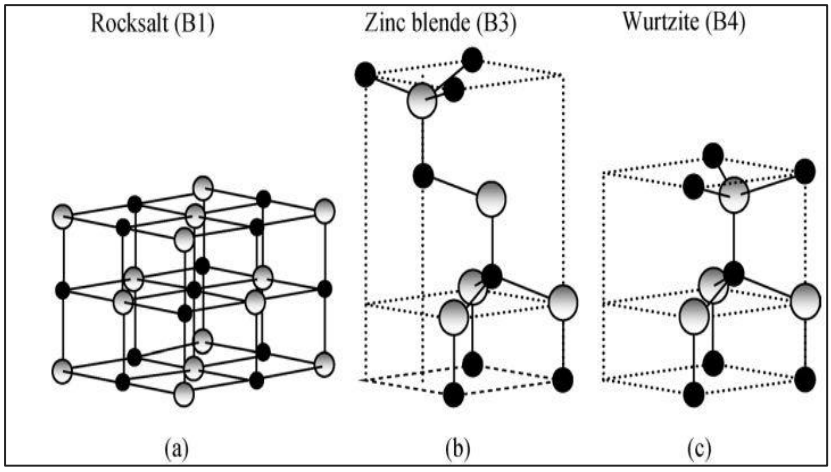

Figure 2.5: Representation of ZnO crystal structures: (a) cubic rocksalt (B1), (b) cubic zinc blende (B3), and (c) hexagonal wurtzite (B4). Shaded gray and black spheres denote Zn and atoms, respectively [40].

The hexagonal wurtzite structure of ZnO is the most common of the three, as it is thermodynamically the most stable. ZnO is biocompatible, biodegradable, and effective for environmental applications. The rock salt phase of ZnO is more densely packed than the Wurtize phase, resulting in a smaller equilibrium for the rock salt phase of ZnO. Wurtzite structure has a higher calculated cohesive energy than rock salt phase, which confirms the Wurtzite is ground state structure in ZnO. A study [41], determined that the lattice constants of as-synthesized ZnO are a = 0.32498 nm, b = 0.32498 nm, and c = 0.52066 nm.

2.5 Synthesis Technique

This section explores production techniques, their influence, and types of procedures. The creation of nanoparticles can occur physically, chemically, or biologically. Various manufacturing methods can result in different nanoparticle properties. Physical procedures involve the breakdown of bigger materials into nanoparticles using mechanical forces or energy, such as high temperatures or pressures. Chemical techniques, on the other hand, involve the use of chemical reactions to synthesize nanoparticles. Biological approaches produce nanoparticles by utilizing living creatures such as bacteria. NPs can have a variety of forms, sizes, and architectures. They can be spherical, cylindrical, conical, tubular, hollow core, spiral, and other shapes, as well as irregular, with the size of NPs can range from 1 to 100 nm[42]. Figure 2.6 below depicts nanomaterials of various dimensions.

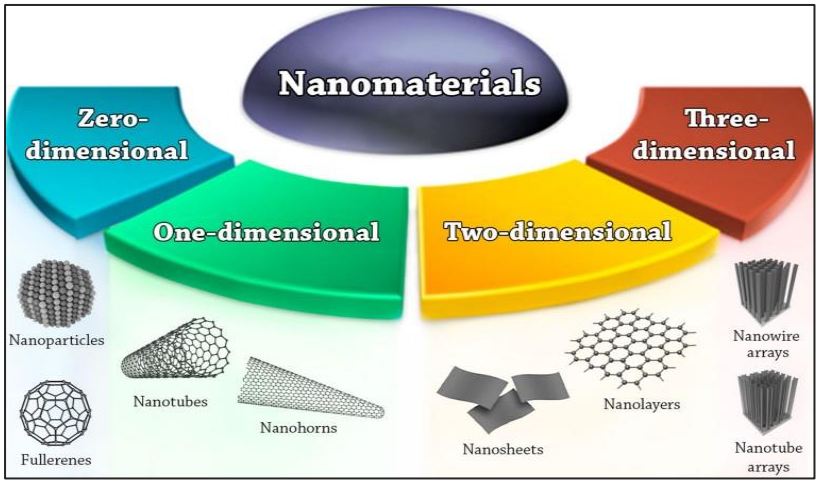

Figure 2.6: Schematic view of nanomaterials of different dimensions[42].

With their distinct shapes, nanostructures have been extensively examined, discussed, and utilized in many technical applications over the past few decades. The development of the controlled synthesis method to produce desired morphology is heavily reliant on the fields of material science and nanotechnology. Several applications in this area can be attributed to ZnO and TiO_2 nanostructures, which are well known for their thermal stability, non-irritating nature, and low cost. General synthesis methods of TiO_2 and ZnO nanostructures shown in figures 2.7.

Figure 2.7: Common Synthetic method of TiO_2 /ZnO Nanostructure[43], [44].

Synthesis technologies play a crucial role in creating nanoparticles. In addition to their unique properties, these materials have applications in medicine, electronics, energy, and materials science. Several promising synthesis technologies have emerged in recent years, enabling controlled and precise production of nanoparticles. The following describes some promising synthesis technologies which is very useful for the synthesis of different nano particles.

2.5.1 Hydrothermal method

The process of making single crystals using hot water under high pressure is known as "hydrothermal synthesis," and it relies on the solubility of minerals in that medium. The crystal growth is performed in an apparatus consisting of a steel pressure vessel called an autoclave (see figure 2.8), in which a nutrient is supplied along with water and a temperature gradient is

maintained between the opposite ends of the growth chamber [45]. This approach allows for greater control over the size, nucleation, and level of crystallinity of the NPs due to the stability afforded by using a closed autoclave system where temperature and pressure are regulated [46].

The hydrothermal method has been utilized to produce a variety of nanostructures, including TiO_2 and ZnO nanostructures, as part of the framework of green synthesis. These structures include monodispersed and highly homogenous NPs, nanohybrid materials, and nanocomposites. Studies have shown that the versatile hydrothermal approach can be utilized to create stable suspensions of doped TiO_2 and ZnO nanostructures with the desired properties.

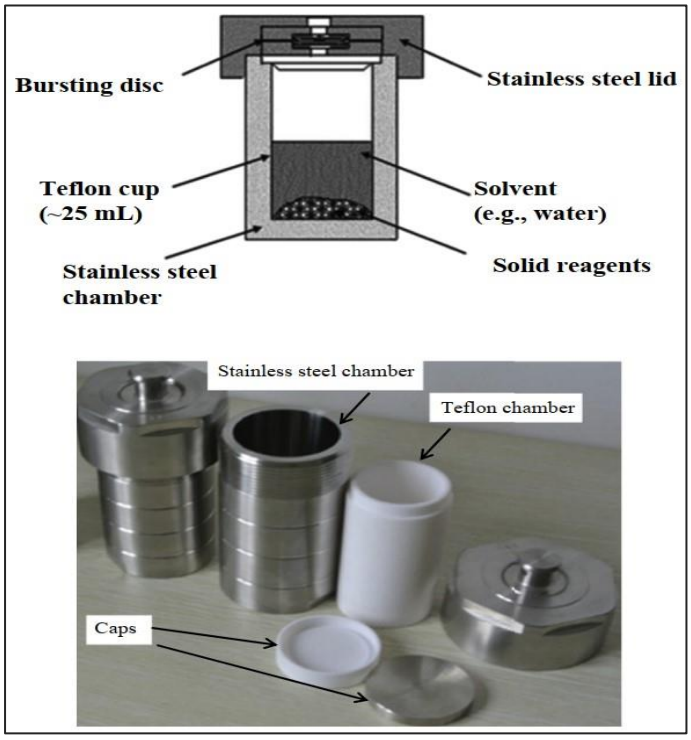

Figure 2.8: Teflon lined stainless steel autoclaves with inner components (upper). The Teflon chamber is housed inside the stainless-steel chamber in which reaction is carried out and the lower image is of the commercially available Teflon lined stainless[45].

2.5.2 Microwave method

Microwave synthesis involves heating the sample at high temperature under electromagnetic irradiation. As a potential technique for green chemistry, microwave synthesis is an alternative to conventional techniques of heating. In comparison to conventional heating (CH), microwave-assisted synthesis (MAS) is often characterized by more selectivity, kinder reaction conditions, and shorter reaction durations [47]. Unlike MAS, where electromagnetic energy is turned into heat by mobile electric charges present in liquid or by conducting ions in solid, CH transfers heat through conduction, convection, or radiation. To quickly produce good yields, microwave radiation is frequently used instead of conventional heating. The research work had shown that this source of energy has been used extensively and successfully in organic synthesis, including in the case of metal-catalyzed synthetic methods and thought to be environmentally benign and, therefore, in accordance with the concepts of green chemistry [47]. The difference between microwave and conventional heating is depicted schematically in figure 2.9.

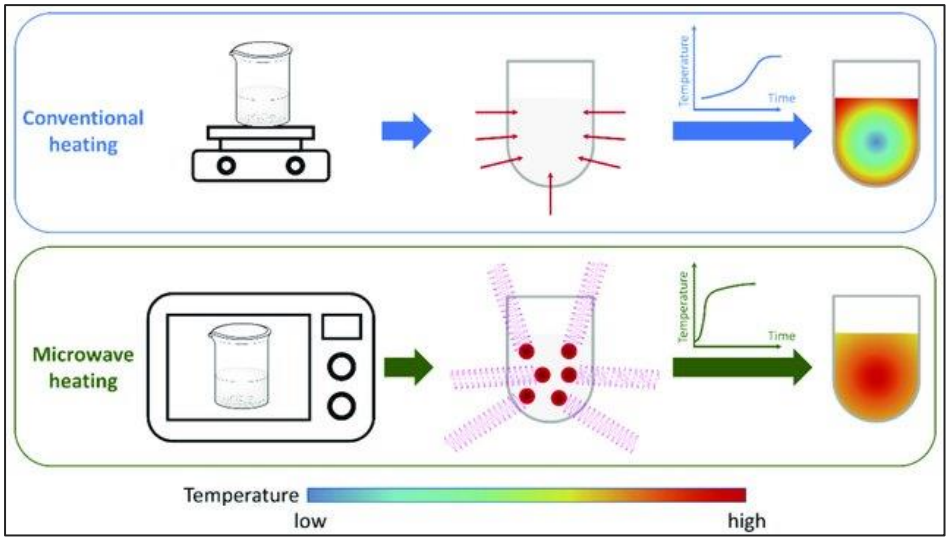

Figure 2.9: Schematic difference between conventional and microwave heating[47] .

2.5.3 Co-precipitation method

Zinc oxide and titanium dioxide nanoparticles (ZnO / TiO_2 NPs) were synthesized as a powder using the co-precipitation method. The simultaneous occurrence of nucleation, growth,

coarsening, and aggregation processes are part of the co-precipitation approach [48]. Nucleation, or the formation of tiny particles, is an important step in the process that can be influenced by factors such as metal ion concentration and solution pH. Secondary processes like Ostwald ripening and aggregation [49] can also have an impact on the size, shape, and properties of the nanoparticles. Ostwald ripening is a process in which smaller particles dissolve and are redeposited onto larger particles, causing the larger particles to grow. The process by which nanoparticles clump together to form larger aggregates, on the other hand, is known as aggregation. Figure 2.10 depicts the usual co-precipitation process for the creation of micro- and nanoparticles.

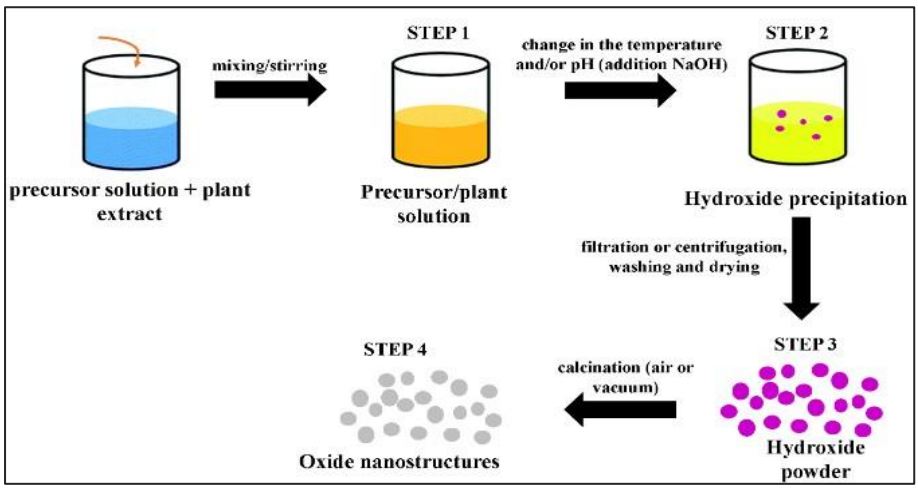

Figure 2.10: Flow sheet for co precipitation technique[44]

Synthesizing metal oxide nanoparticles from plant extracts is a complex and multi-step process. The first stage includes vigorously mixing the precursor solution with the plant extract solution, followed by control manipulation of the temperature and pH by adding NaOH, which commences the precipitation process and promotes the creation of hydroxides. The residue is then carefully separated from the solution using either a simple centrifugal technique, and properly washed with deionized water and ethanol. The purity and quality of the resultant nanoparticles are increased by washing the residue with deionized water and ethanol, ensuring that they have desirable features that are necessary for many applications, such as biocompatibility, stability, and functionality The residue is then dried at low temperatures to assure a pure and consistent product. The ultimate and most crucial part of the process is the

calcination of the metal oxide, a heat treatment that releases nanoparticles with a distinct metallic smell and precise crystalline structures. The resulting nanoparticles can be further treated by grinding them to a fine, silky powder with a crystal mortar and pestle.

2.5.4 Thermal decomposition and air plasma method

Pyrolysis or thermal decomposition as one of the best methods to synthesize stable, monodisperse metal nanoparticles and small particle size [50]. Pyrolysis is a thermochemical process in which a substance breaks down into smaller components in the absence of oxygen. However, air plasma method is promising technology for the creation of different nano particles. The advantages of the air plasma method are shorter process cycle and suitability for more complex medical instruments [51]. In order to produce charged particles (free radicals), gas molecules are excited using radio frequency or microwave energy in this air plasma technique [51].

2.5.5 Physical vapor deposition (PVD) and Chemical vapor deposition (CVD)

Physical vapor deposition techniques, also known as thin film techniques or atomistic deposition techniques in which material is vaporized from a solid or liquid source in the form of atoms or molecules and transported through a vacuum or low pressure gaseous (or plasma) environment to the substrate, where it condenses [52]. PVD methods can be used to create multilayer coatings, graded composition deposits, extremely thick deposits, and freestanding structures in addition to depositing films with thicknesses between a few nanometers and thousands of nanometers [52]. Vah et al in 2019 reported photocatalytic efficiency of TiO_2 by PVD method [53]. On the other hand, Chemical vapor deposition refers to the deposition of a solid on a heated surface from a chemical reaction in the vapor phase[54]. Additionally, in 2010 Lupan and colleagues reported the synthesis of ZnO nanowires using chemical vapor deposition (CVD) at a temperature of 650°C [55]. Moreover, TiO_2 nanowires and nanowalls core structures covered with carbon shell were synthesized by a CVD method using commercial titanium powder as the starting material[56]. Thus, CVD and PVD are both important tools in the manufacturing of a wide range of products, and they have numerous applications in fields such as electronics, automotive, aerospace, and medical devices.

2.5.6 Sol-gel method

A sol-gel method is a versatile approach that entails making a sol, a colloidal suspension of nanoparticles, and then gelating the sol to produce a solid. The sol-gel process typically begins with a precursor solution, a liquid mixture containing the reactants that eventually form the sol-gel. The precursor solution is then aged or matured over time, typically at room temperature, allowing the reactants to fully dissolve and react with each other. The aging process can take several hours to several days, depending on the specific reactants and conditions. The resultant gel is then dried to form a solid that may be crushed into a powder. After that, the powder can be calcined, or heated to a high temperature, to eliminate any remaining solvent and sinter the nanoparticles together. The sol-gel process precisely controls the nano particles' size, shape, and chemical content, which can influence their photocatalytic activity. Figure 2.11 shows a schematic overview of the sol-gel process.

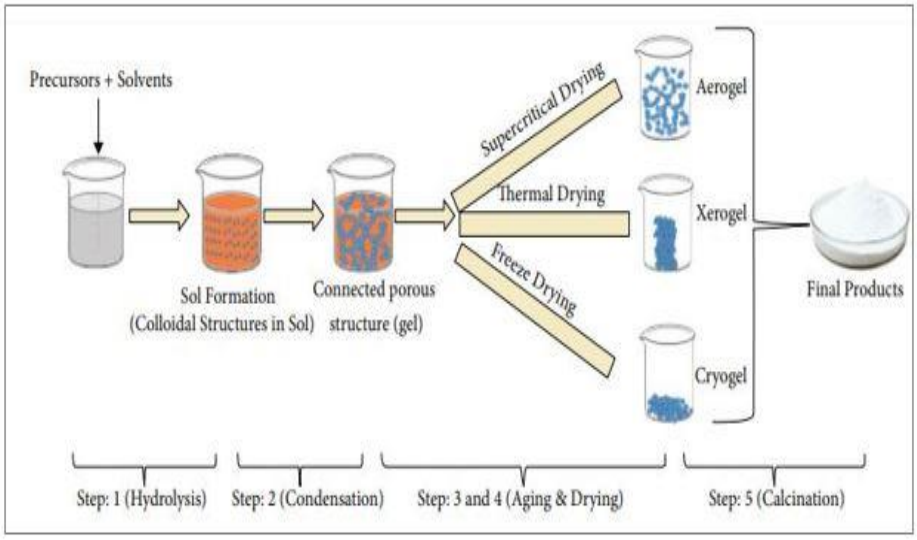

Figure 2.11: Schematic of different stages of sol-gel process: from precursor to aerogel [57].

3 Materials and Methods

3.1 Chemicals

Table 3.1: Summarizes the chemicals applied in this experiment.

No.	Chemicals	Description	Stored Place
1	Zinc acetate dehydrate ($Zn((CH_3COO)_2 \cdot 2H_2O)$)	EMSURE ACS, CAS-NO: 5970-45-6, Germany	USN Lab
2	Titanium dioxide (TiO_2)	Sigma Aldrich, 634662, 99.5% trace metal basis, <100 nm particle size	USN Lab
3	Zinc oxide (ZnO)	Sigma Aldrich	USN Lab
4	Methyl orange ($C_{14}H_{14}N_3SO_3Na$)	Sigma Aldrich, 114510, Merck Life Science AS	USN Lab
5	Ethanol (C_2H_5OH)	Ethanol absolute AnalaR NORMAPUR® Reag. Ph. Eur., Reag. USP, ACS , 20821	USN Lab
6	Sodium dodecylsulfate (SDS) ($C_{12}H_{25}NaO_4S$)	Sigma-Aldrich, 436143, Merck Life Science AS	USN Lab
7	Hydrochloric acid (HCL)	Hydrochloric acid 37% AnalaR NORMAPUR® Reag. Ph. Eur, 20252	USN Lab
8	Titanium (IV) butoxide ($C_{16}H_{36}O_4Ti$) or $Ti(C_4H_9O)_4$	Sigma Aldrich, 244112, Merck Life Science AS	USN Lab
8	Biochar	Biochar from Standard Bio AS, Telemark, Norway	USN Lab

3.2 Instruments

Table 3.2: Various instrument types and the firms available at USN lab

No.	Instruments	Company	Place
1	Centrifuge Machine	CORNING/ LSE,230 V, EU, High speed Micro centrifuge	USN Lab
2	Temperature Chamber	Lenton ,202	USN Lab
	Ultra-Sonic Bath	FinnSonic, FIN-15170 Lahti	USN Lab
3	U-Vis Spectrophotometer	UV-2600, SHIMADZU	USN Lab
4	Scanning Electron Microscope (SEM)	SEM Hitachi SU 3500	USN Lab
5	X-Ray Diffractometer (XRD)	XRD Thermo Ficher Equinox 1000	USN Lab
6	Fourier Transform Infrared Spectroscopy (FTIR)	Thermo Fischer, Nicolet iS50	USN Lab

3.3 Methyl orange

3.3.1 Molecular composition and chemical formula

Methyl Orange is commercially produced through chemical synthesis and is primarily obtained from chemical suppliers and manufacturers. The exact steps of the synthesis process can differ, but it typically involves the carefully monitored combination of selected precursor molecules. To assure the reproducibility and quality of the manufactured methyl orange, chemical

manufacturers adhere to defined protocols. This enables its commercialization for a variety of industrial applications, such as dyeing, pH indicator use, and research. Methyl orange (MO) [$C_{14}H_{14}N_3SO_3Na$] is one of the most ordinary dyes. Figure 3.1 shows its molecular composition and chemical formula. The IUPAC name for MO is 4-dimethylaminoazobenzene-4'-sulfonic acid sodium salt. Figure 3.2 depicts the absorption spectra of a 5x 10^{-5} mol/L solution of methyl orange in water, which has a broad absorption band with a maximum wavelength of 465 nm and an intensity of 1.018 [58].

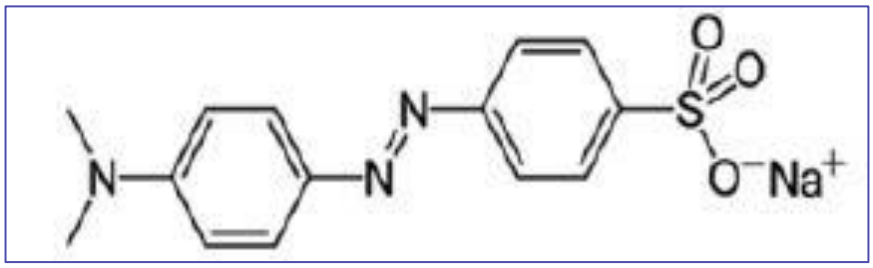

Figure 3.1: Molecular Structure of Methyl Orange [65]

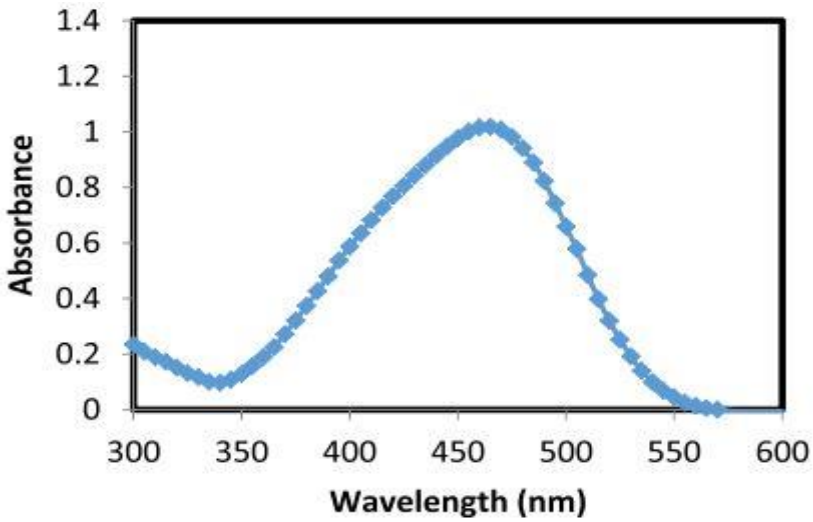

Figure 3.2: Absorption Spectrum of Methyl Orange Solution of Methyl Orange [59].

3.3.2 Application of methyl orange

Methyl orange is widely used as a dye in textile, leather, and paper industries. Its brilliant orange colour gives vitality to various materials, including fabrics, leather goods, and paper. In contrast, it is used as a pH indicator in laboratories and industries. Around pH 3.7, the colour

changes from orange (acidic conditions) to yellow (alkaline conditions). This makes it useful for detecting the acidity or alkalinity of solutions during titrations and other chemical operations.

While methyl orange has huge industrial applications, its presence in wastewater can cause environmental contamination and destroy aquatic habitats. As a result, effective disposal and wastewater treatment are critical to minimizing the detrimental effects of its industrial applications[60].

3.4 Preparation of a stock solution

Stock solutions are concentrated solutions with known, and accurate concentrations that is diluted for use in laboratory. The preparation of stock solutions can help experimental operation run more smoothly and save a lot of time and resources.

The basic relationship for dilution is,

$$C_1 \text{ x } V_1 = C_2 \text{ x } V_2 \tag{3.1}$$

Here,

C_1 is the concentration of stock.

V_1 is the volume of stock.

C_2 is the concentration of diluted. i.e., 2, 4, 6, 8, 10, 12,14,16,18, and 20 ppm solution for respective dilution standards

V_2 is the volume of diluted.

In general,

$$\text{Volume from stock to be taken} = \frac{\text{Required concentration x Required volume}}{\text{Stock}} \tag{3.2}$$

To prepare MO solutions of different concentrations, a 20 ppm MO stock solution was first prepared by dissolving 0.010 g of MO powder in 500 ml of deionized water in a flask. From this stock solution, MO solutions of 2 ppm, 4 ppm, 6 ppm, 8 ppm, 10 ppm, 12 ppm, 14 ppm, 16 ppm, and 18 ppm were prepared as follows. For a 2 ppm MO solution, 2 ml of the 20 ppm MO stock solution was measured and added to a 20 ml flask, followed by the addition of 18 ml of deionized water. Similarly, for a 4 ppm MO solution, 4 ml of the stock solution was added to 16 ml of deionized water in a 20 ml flask. For a 6 ppm MO solution, 6 ml of the stock solution

was added to 14 ml of deionized water, and so on. After adding the appropriate amount of MO stock solution to the flask, the total volume was brought up to 20 ml by adding deionized water. Each solution was then mixed thoroughly by shaking or stirring, as appropriate, until the MO was completely dissolved. The resulting solutions were used for further experiments as needed.

Figure 3.3:Stock solution (20ppm) prepared in a fume hood of USN lab.

3.5 Preparation of materials

In the present study, TiO_2 and ZnO nanoparticles as well as their composites were synthesized using different experimental techniques. The nanoparticles and composites were then analyzed using various characterization methods to understand their physical and chemical properties.

3.5.1 Preparation of TiO_2 nanoparticles

The synthesis of TiO_2 nanoparticles was improved by incorporating a hydrothermal treatment step. The initial synthesis involved dissolving SDS (sodium dodecyl sulphate) (0.68 gm) in a solution of water (150mL). After stirring for 30 minutes at 50°C, Titanium (IV) butoxide (10ml) and 2M HCl acid solution were added drop by drop and the mixture was stirred for an

additional 2 hours. The mixture was then transferred for hydrothermal treatment at 140°C for 24 hours. The resulting sample was collected by centrifugation (3000rpm for 20minutes), washed with ethanol by oil batch method at 80^0C for 24 hours as illustrated by figure 3.4, this process repeated 3 times until removed all the SDS from the TiO_2 nanoparticles, and dried 24hours at 80°C and finally crushed by using mortar and pestle to get TiO_2 NPs powder.

Figure 3.4:Visualization of oil batch through ethanol washing and heat treatment.

.

3.5.2 Preparation of BC/prepared TiO_2 nanocomposites

To prepare the composite material, equal amounts (0.1 g each) of prepared TiO_2 nanoparticles and biochar were dispersed in separate 50 mL aliquots of ethanol. The biochar-ethanol mixture was then subjected to ultrasonic treatment for 30 minutes to ensure uniform particle dispersion. This was followed by stirring the TiO_2-ethanol solution magnetically for 30 minutes to maintain homogeneity and prevent the settling of TiO_2 particles during the reaction. The two solutions were then mixed and allowed to stir magnetically for an additional 2 hours to ensure complete mixing. Subsequently, the mixture was transferred to an autoclave and heated to 140°C for 24 hours in a temperature chamber to facilitate the formation of the composite material (see equation 3.3).

$$TiO_2 + \text{biochar} \rightarrow TiO_2\text{-biochar} \quad (3.3)$$

After autoclaving, the composite material was subjected to a centrifugation-based purification process using the centrifuge machine as shown in figure 3.5. The precipitates obtained after

centrifugation was washed with deionized water and centrifuged again to remove any remaining impurities. This washing process was repeated thrice to eliminate any particles that could affect the performance of the composite material in subsequent experiments ensuring that only high-quality material was used in the experiments. Finally, the material was dried in an oven for 24 hours and crushed into a fine powder for subsequent analysis and experimentation.

Figure 3.5: Sample inside centrifuge machine [Steinberg system SBS -LZ-4000 / 20 -12] for centrifugation process at USN lab.

3.5.3 Preparation of ZnO nanoparticles

Zinc oxide nanoparticles were prepared in the lab by dissolving 6 g of zinc acetate dihydrate ($Zn(CH_3COO)_2 \cdot 2H_2O$) in 150 mL of ethanol. The mixture was stirred for 30 minutes until they were completely dissolved. Separately, 0.2 g of sodium hydroxide (NaOH) were dissolved in 150 milliliters of ethanol, and the solution was also stirred for 30 minutes to ensure complete dissolution. The sodium hydroxide and ethanol solution were added dropwise to the zinc acetate dihydrate and ethanol mixture while stirring continuously for 2 hours. The mixture was then transferred to a stainless-steel autoclave system and incubated at 80 ^{0}C for 24 hours. After the incubation period, the solution was removed from the autoclave system and centrifuged to separate the nanoparticles from the solution. The precipitate was washed three

times with deionized water and dried at 80°C for 24 hours to obtain the zinc oxide nanoparticles.

3.5.4 Preparation of BC/ZnO nanocomposites

To prepare the zinc oxide biochar, 0.2 g of biochar obtained from Standard Bio AS, Telemark, Norway was mixed with 100 mL of ethanol and stirred using a magnetic stirrer for 30 minutes. Separately, 0.2 g of zinc acetate dihydrate were dissolved in 100 mL of ethanol and stirred using a magnetic stirrer for 30 minutes to obtain a clear solution. The addition of the zinc acetate dihydrate and ethanol solution dropwise to the biochar and ethanol solution while stirring continuously for 2 hours using a magnetic stirrer facilitated the attachment of the zinc oxide nanoparticles to the biochar surface, resulting in the formation of zinc oxide biochar. The resulting solution was then transferred to a stainless-steel autoclave system and incubated at 80°C for 24 hours. After the incubation period, the solution was removed from the autoclave system and the nanoparticles were isolated by centrifugation. The precipitate was washed three times with deionized water to remove any remaining impurities. The washed zinc oxide biochar nanoparticles were dried at 80 degrees Celsius for 24 hours to obtain the final product.

3.5.5 Preparation of BC/ prepared ZnO nanocomposites

Standard Bio AS BC (0.2 g) was combined with ethanol (100 mL) and stirred for 30 minutes. After 30 minutes of stirring, prepared ZnO (0.2 g) was dissolved in ethanol (100 mL), yielding a simple solution. The ZnO solution was added to the BC solution and agitated for 2 hours. The mixture was incubated at 80°C in a stainless-steel autoclave for 24 hours. After incubation, the nanoparticles were recovered by centrifugation, washed three times with deionized water, and dried at 80°C for 24 hours to produce the BC-ZnO composite.

3.5.6 Preparation of BC/ commercial ZnO nanocomposites

The procedure for preparing BC/commercial ZnO nanocomposites is similar with that of making BC/prepared ZnO nanocomposites. Standard Bio AS biochar (0.2 g) was mixed with 100 mL of ethanol and stirred with a magnetic stirrer for 30 minutes. Separately, 0.2 g of ZnO from

Sigma Aldrich was dissolved in 100 mL of ethanol, forming a clear solution after 30 minutes of magnetic stirring. The ZnO solution was then added to the biochar and stirred for 2 hours. The resulting solution was transferred to a stainless-steel autoclave and incubated at 80°C for 24 hours. After incubation, the nanoparticles were isolated through centrifugation and washed three times with deionized water to remove impurities. Finally, the zinc oxide-biochar nanoparticles were dried at 80°C for 24 hours to yield the final product.

The process can be represented by,

$$BC + ZnO \rightarrow BC\text{-}ZnO \quad (3.4)$$

Where, BC represents biochar and ZnO represents zinc oxide. The final product is a composite of biochar and zinc oxide.

3.5.7 Preparation of BC/commercial TiO_2 nanocomposites

The process of synthesizing Titanium dioxide-biochar nanoparticles using a solvent-assisted autoclaving method was performed, following a similar procedure to that used for the preparation of commercial ZnO biochar. Initially, 0.2 g of Standard Bio AS biochar was mixed with 100 mL of ethanol and stirred for 30 minutes using a magnetic stirrer. Separately, 0.2 g of titanium oxide from Sigma Aldrich was dissolved in 100 mL of ethanol and stirred for 30 minutes until a clear solution was obtained. The titanium oxide solution was then added to the biochar and stirred for 2 hours to allow for the formation of nanoparticles. The resulting solution was then transferred to a stainless-steel autoclave and incubated at 80°C for 24 hours. Following incubation, the nanoparticles were isolated by centrifugation and washed three times with deionized water to remove any remaining impurities. Finally, the washed titanium oxide-biochar nanoparticles were dried at 80°C for 24 hours to obtain the final product.

3.6 Characterization Technique

Several procedures were used to investigate the final sample of TiO_2 and ZnO and their composites to determine their crystal structure, shape, size, and light absorption properties. These characterization approaches provided a comprehensive insight into the crystal structure, form, dimensions, and light absorption properties of TiO_2, ZnO, and their composite

samples. These findings were critical for determining the materials' feasibility for photocatalytic applications and their capacity for decomposing organic molecules such as methyl orange under light irradiation.

3.6.1 X-ray Diffraction (XRD)

To accurately determine the materials' structures in the field of materials world, X-ray diffraction (XRD) (see figure 3.6) method is frequently employed as a fingerprinting instrument. In this study, the crystalline structure of the synthesized ZnO as well as TiO_2 powders and their composites was analyzed by XRD Thermo Ficher Equinox 1000 at USN lab with Cu Kα radiation (λ = 1.540 Å) at 40 kV and 30 mA. XRD pattern is created when incident X-rays interact with the crystal planes of the material structure. However, constructive interference of X-rays is possible only at certain angles, which depend on the wavelength of the incident X-rays and the distance between planes in the crystal structure, according to the Bragg's law relationship,

$$n\lambda = 2\,d\sin\theta \tag{3.5}$$

Equation (3.8) relates four variables: n, an integer; d, the interplanar spacing or distance; λ, the incoming wavelength of X-rays; and θ, the angle of incidence. Figure 3.6 explains Bragg's law.

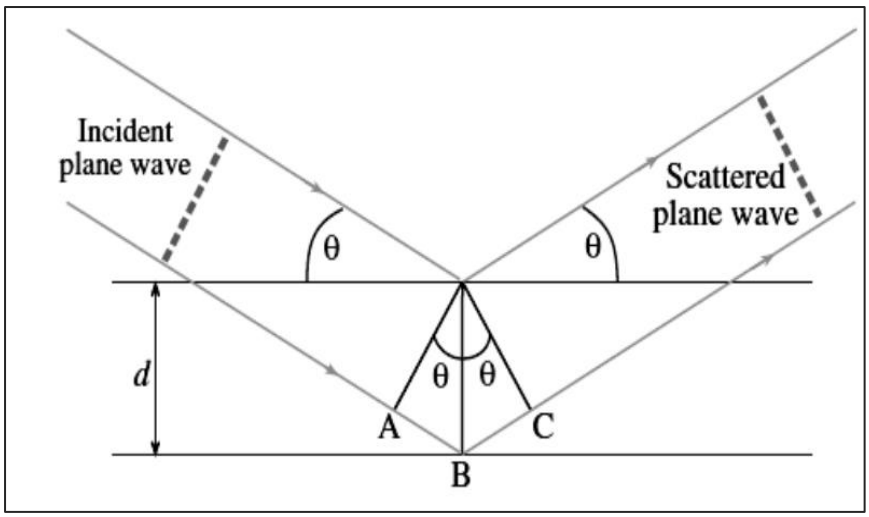

Figure 3.6: Illustration of Bragg's law [61].

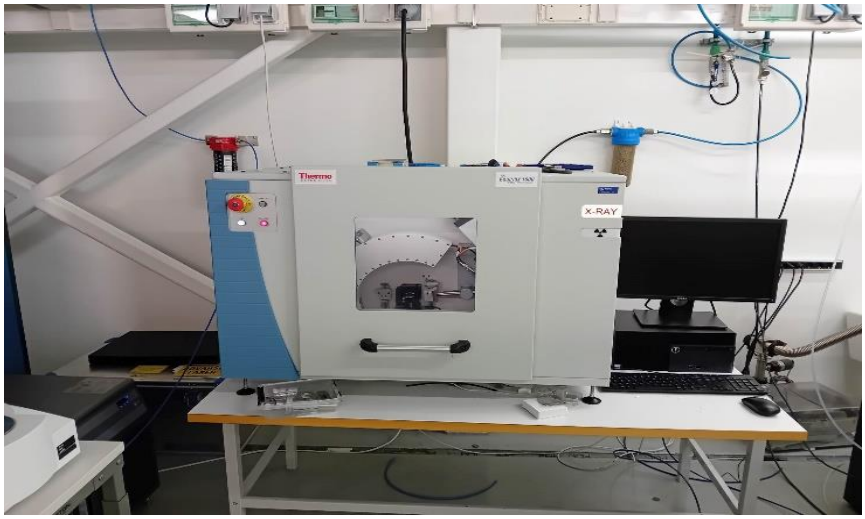

Figure 3.7: XRD machine at USN lab

3.6.2 Scanning Electron Microscope-Energy Dispersive X-ray Spectroscopy (SEM-EDS)

Scanning Electron Microscopy with Energy-Dispersive Spectroscopy is abbreviated as SEM-EDS. It is a technique that combines SEM imaging with EDS chemical analysis. SEM uses an electron beam to scan a surface morphology of sample, and the interactions between the electrons and the sample's atoms produce an image of the specimen surface. Through SEM-EDS, researchers can study how materials change after being exposed to light. The NPs composition as well as biochar was determined using a SEM Hitachi SU 3500 (see figure 3.8).

The initial characterization was performed to determine the composition of the zinc oxide, titanium dioxide as well as biochar and to validate the stoichiometric presence of these elements. If the sample contains TiO_2 and ZnO nanoparticles, the presence of these elements should be visible in the SEM image and the EDS spectrum. A researcher can see individual nanoparticles or clusters of NPs in the SEM image. Peaks in the EDS spectrum should correspond to the characteristic energies of the elements present in the sample, including Ti, O, Zn, and O. By comparing the intensities of these peaks to known standards, analyst should be able to confirm the presence of TiO_2 and ZnO in the sample.

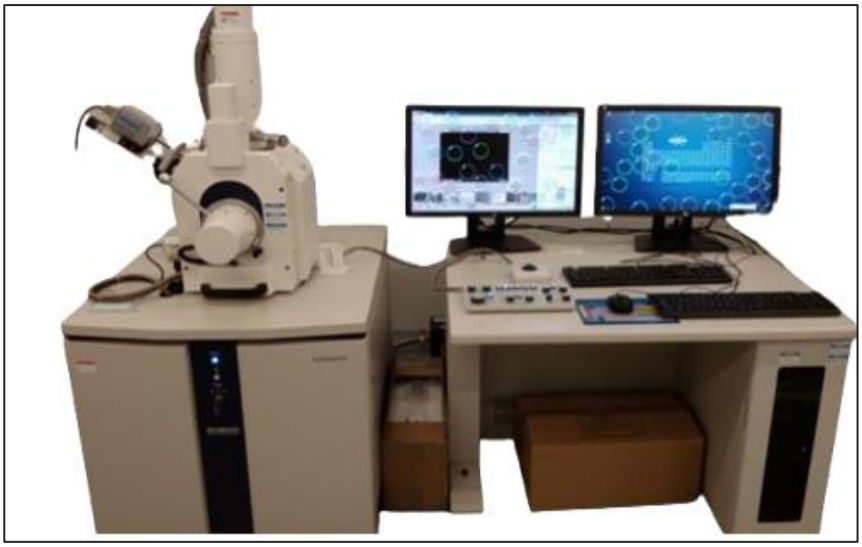

Figure 3.8: Pictorial view of SEM Hitachi SU 3500 at USN lab.

3.6.3 Fourier transform spectroscopy (FTIR)

FTIR spectroscopy uses infrared light to observe the chemical bonds between molecules and to explore their vibrational and rotational behavior. Chemical bonds in a sample absorb specific wavelengths of infrared light, resulting in distinct absorption peaks. By measuring the absorbed frequencies, FTIR spectroscopy identifies the types of bonds in the selection and assists in determining their molecular structure and composition.

This method is widely used in materials science to study the properties of various materials such as ZnO, TiO_2, and biochar. Our study uses FTIR to analyze chemical functional groups in biochar, TiO_2, and ZnO. Figure 3.9 shows the schematic layout of FTIR of the USN lab (Manufacturer: Thermo Fischer with Model: Nicolet iS50). We get useful insights into the chemical composition and bonding features of biochar, TiO_2, and ZnO by using FTIR. This knowledge improves our understanding of the properties and possible applications of these materials in domains such as environmental science, energy, and catalysis.

Figure 3.9: Pictorial view of FTIR at USN lab.

3.6.4 UV-visible (UV-Vis) spectrophotometry

UV-visible (UV-Vis) spectrophotometers are essential for materials applications and photocatalytic processes. A fundamental spectroscopy principle is that compounds absorb ultraviolet or visible light to produce a distinct pattern. Electron-optical transitions between valence and conduction bands are responsible for the generation of the spectrum.

The interaction of light and matter is the basis of UV-Vis spectrophotometry. Methyl orange dye, the test dye we utilized in this experiment to assess the photocatalytic capabilities of ZnO and TiO_2 by the UV-Vis spectrophotometer. The SHIMADZU UV-2600 Spectrophotometer (see figure 3.10) was used in this research to record the UV-Vis transmission spectra of the synthesized ZnO as well as TiO_2 over the wavelength range of 200-800nm to study the photocatalytic behavior. Using the same tools, the UV-Vis absorption spectra of MO solutions were also obtained.

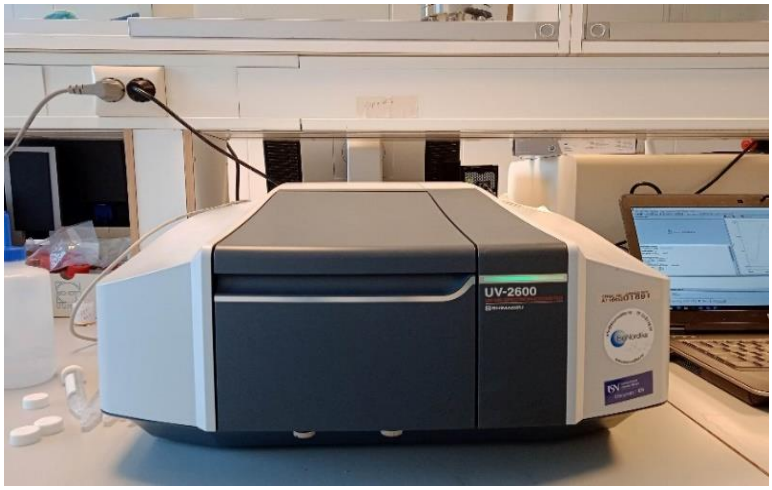

Figure 3.10: Digital Photography of Ultra-violet Visible Spectrophotometer (UV-Vis) at USN

3.7 Photodegradation Kinetic Tests

Photodegradation kinetic tests are a powerful tool for assessing the potential impact of chemical compounds on the environment. In the laboratory, these experiments evaluate the chemical compound's rate and extent of degradation when exposed to light. By monitoring samples over time and analyzing the resulting data, key parameters such as rate constant and half-life can be calculated, allowing for the assessment of the kinetics of the degradation process. In this experiment, both first and second-order kinetic test models were utilized, providing a comprehensive understanding of the photodegradation process of methyl orange. The degradation of MO through photodegradation can be described by first-order kinetics, where the rate of the reaction is directly proportional to the concentration of MO in the solution (C_t).

The equation can be expressed as,

$$\ln(\frac{C_0}{C_t}) = \mathrm{kt} \tag{3.6}$$

On the other hand, The pseudo-second order kinetics model can be expressed in the following form[62], [63]:

$$\mathrm{t/q_t} = 1/\mathrm{K(q_e^2)} + \mathrm{t/(q_e)} \tag{3.7}$$

Where,

t is the reaction time, q_t (mg g^{-1}) is the amount of methyl orange adsorbed at time t, K (g mg^{-1} $min^{-1)}$ is the pseudo second order rate constant, q_e (mg g^{-1}) is the amount of methyl orange adsorbed at the equilibrium. By rearranging this equation, we obtained a linear plot of t/qt versus t, which resulted in a straight line with a slope of $1/q_e$ and a y-intercept of $1/Kq^2_e$. The values of K and q_e were obtained by measuring the y-intercept and slope of the line, respectively.

$$q_t = V_s (C_o - C_t) / (W) \quad (3.8)$$

$$q_e = V_s (C_0 - C_e) / (W) \quad (3.9)$$

where C_0, C_e and C_t are the initial, equilibrium and instantaneous dye concentrations respectively. Vs is the volume of the aqueous solution and W is the amount of catalyst. By conducting first-order and second-order kinetic tests, it is possible to identify whether the experimental data follows a first-order or second-order reaction rate law and calculate the rate constant that characterizes the rate of the reaction under the specific conditions. This information can be helpful in comprehending the reaction mechanism, optimizing reaction conditions, and predicting the behavior of the reaction under different circumstances.

3.8 Photocatalytic Measurements

In this experiment, the Beer-Lambert Law is used to determine the absorbance of a compound in a photocatalytic solution. Analyzing variations in absorbance allows us to evaluate photocatalytic progress and efficiency. These experiments are frequently performed with a spectrophotometer, which measures the absorbance of the solution at a given wavelength. The Beer-Lambert Law [64] states that the absorbance of a solution is directly proportional to the concentration of the compound in the solution.

i.e, $A = \varepsilon b C$ (3.10)

where A is absorbance (no units), ε is the molar absorptivity (L $mol^{-1}cm^{-1}$), b is the path length of the sample solution in the cuvette (cm), and C is the concentration of the compound in the solution (mol L^{-1}).

The photodegradation efficiency[65] was calculated using relation,

$$\% \text{ Degradation} = \frac{Co-C}{Co} \text{ x } 100 = \frac{Ao-A}{Ao} \text{ x } 100 \quad (3.11)$$

Here, C_0 and C represent the dye's initial and post-irradiation concentrations, respectively, and A_0 and A represent the absorbance of MO solution at 464nm as measured by the UV-Vis.

Equation 3.5 can be written as,

$$\% \text{ Degradation} = [\ 1 - \frac{A}{Ao}] \text{ x} 100 \quad (3.12)$$

Dividing equation (3.4) by bc, we get,

$$\frac{A}{bc} = \varepsilon \quad (3.13)$$

Typically, the path length of the cuvette is 1 cm, and the slope is equal to ε, resulting in the equation, $C = \frac{A}{\varepsilon} = \frac{A}{\text{slope}}$ (3.14)

where, $\text{slope} = \frac{A}{C}$

4 Results and Discussion

This section thoroughly examines the numerous characterization techniques used to analyse materials' structure, morphology, characteristics, and photocatalytic degradation. XRD (X-ray Diffraction), SEM-EDS (Scanning Electron Microscopy-Energy Dispersive X-ray Spectroscopy), FTIR (Fourier Transform Infrared Spectroscopy), and UV spectroscopy are all covered in this chapter. These technologies provide critical vital insights into the properties and behaviour of materials, which aids in their comprehension and prospective applications.

4.1 XRD analysis of TiO_2 nano particles and its composites

The XRD analysis of biochar (BC), commercial titanium dioxide (TiO_2), commercial titanium dioxide biochar (TiO_2/BC) nanocomposite, commercial zinc oxide (ZnO), and commercial zinc oxide biochar (ZnO/BC) nanocomposite materials is depicted in figure 4.1. A detailed analysis of the crystal structure and composition of materials was conducted using X-ray diffraction (XRD). Figure 4.1 shows XRD patterns with significant diffraction peaks at 27° at peak (101) and (211) at 55° suggesting TiO_2 in rutile phase which is supported by research work done by Thamaphat et al [66] and the small peaks mentioned, such as (002), (004), (200), (105), (211), (204), and (220), are indicative of additional crystallographic planes or reflections in the XRD pattern. Titanium dioxide (TiO_2) was identified to possess a rutile phase crystalline structure and a tetragonal crystal system with cell size parameters of a=4.584 Å and c=2.593 Å, using the Powder Diffraction File (PDF) database from Match! 1.11k software (PDF 01-089-4920). As shown in figure 4.1, the similarity of XRD peaks at locations (101), (002), (004), (200), and (211) of commercial TiO_2 and commercial TiO_2 and BC nanocomposites (BC/TiO_2) demonstrates that both materials have similar crystal structures and diffraction patterns.

Similarly, the crystal system of ZnO was determined to be hexagonal, with lattice parameters of a=3.2495 Å and c=5.2069 Å (PDF 03-065-3411). The XRD peaks for ZnO and ZnO biochar were found to be strikingly similar, indicating a high degree of similarity in their crystal structures. The synthesized materials were identified as ZnO in the wurtzite phase, and their X-ray diffraction (XRD) pattern exhibited excellent agreement with the reported JCPDS data [67]. All these observed peaks, including (100), (101), (002), (102), (110), (103), (112), (201),

corresponded to the expected positions for ZnO in the wurtzite crystal structure, providing strong evidence of ZnO. The absence of any significant additional peaks or impurities confirms the high purity of the ZnO sample. Several possibilities for ZnO's potential applications in electronics, photonics, and sensing have been explored by these findings. In conclusion, the similarity between the XRD peaks of ZnO and ZnO biochar, as well as TiO_2 and TiO_2 biochar, provides intriguing insights into these materials. Biochar can be used as a matrix for a wide range of functional materials, providing a platform for enhancing their properties and developing novel applications. Further research and meticulous investigation are warranted to elucidate the underlying mechanisms and implications of these findings.

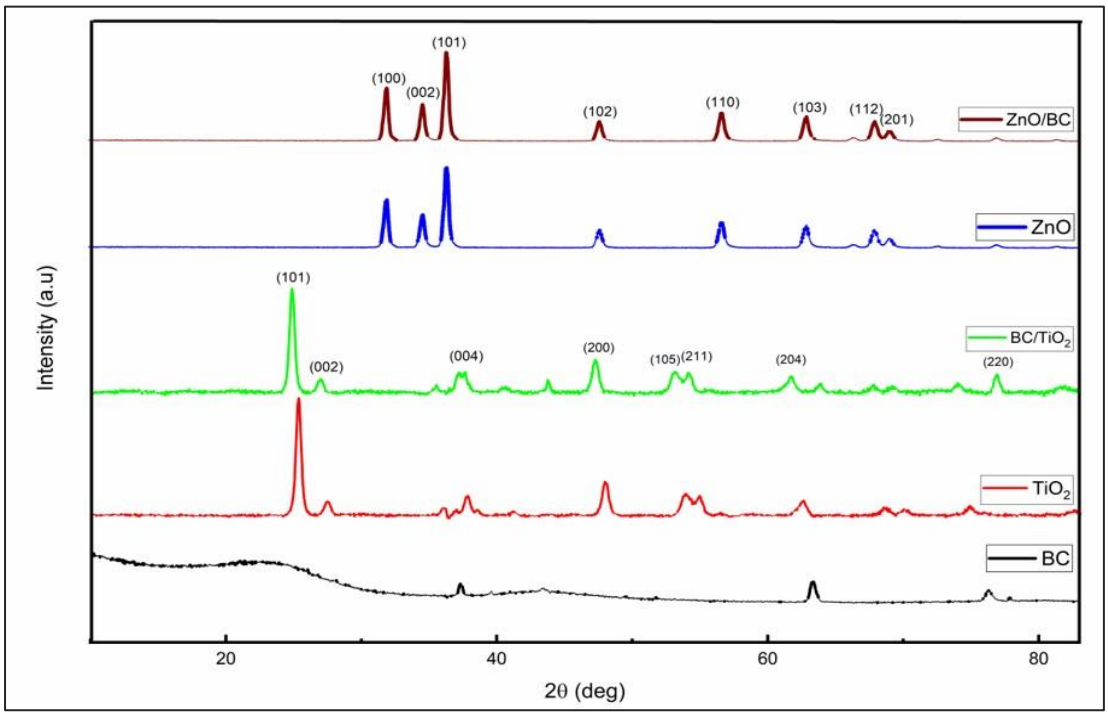

Figure 4.1: XRD analysis of commercial samples with its composites

The XRD analysis for prepared nano particles with its composites is illustrated below figure 4.2. The data obtained from the TiO_2 samples, including both prepared TiO_2 and prepared TiO_2 biochar, exhibit the presence of both anatase and rutile phases. The X-ray diffraction (XRD) patterns show well-defined peaks for each phase, with the anatase phase being characterized by the 25.28° and 37.3° peaks (corresponding to the (101) and (004) crystallographic planes, respectively) according to the JCPDS Card no. 21-1272 which is supported by work done by [67] However, peak (210) and (202) characterized the rutile phase as for value of peak by 43.0° and 77.5° respectively Match! 1.11k software (PDF 01-078-2435). The X-ray diffraction pattern

of ZnO shows multiple distinct peaks at different crystallographic planes. The hexagonal (wurtzite) structure of ZnO is consistent with the peaks (100), (002), (101), (102), (110), (103), (200), (112), and (201). Notably, the preferred orientation of the crystal structure is along the (101) plane, implying that the ZnO crystallites in the sample are mostly aligned in this direction. These findings accord with the reference data from JCPDS Card No. 01-075-1526 [68], which is widely recognized as a standard reference for ZnO XRD patterns.

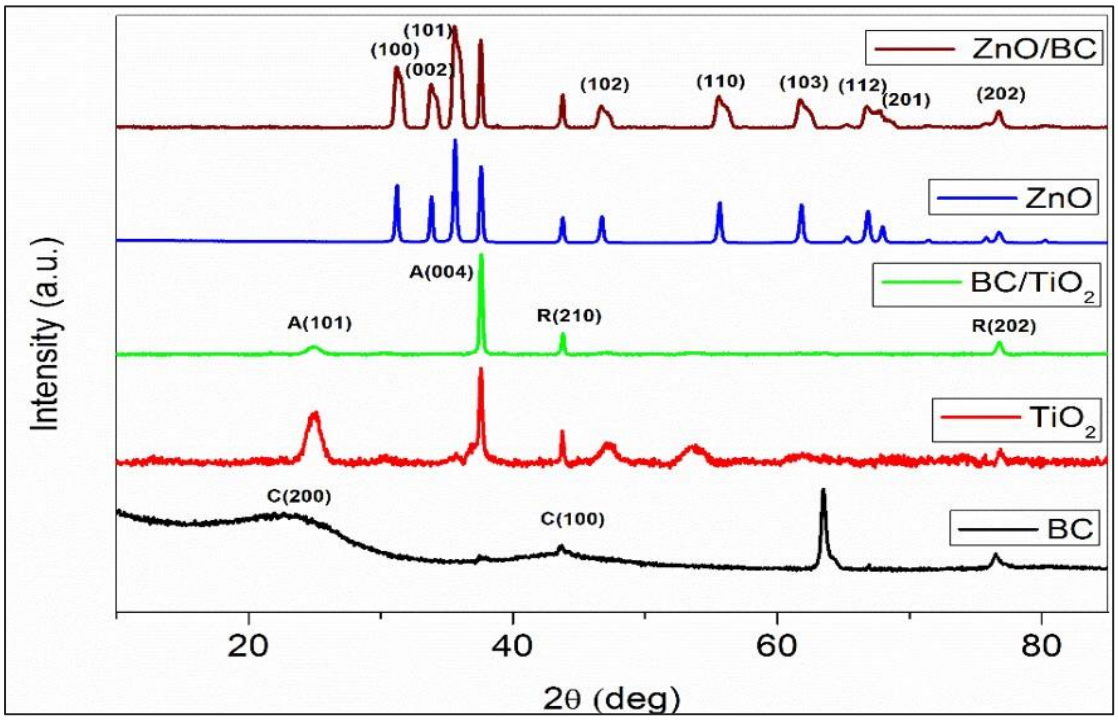

Figure 4.2: XRD analysis for prepared samples with its composites.

4.2 SEM-EDS analysis of BC, TiO_2/BC and ZNO/BC composites

This section provides result obtained from SEM-EDS of TiO_2/BC, and ZnO/BC nano composites. The analysis serves as a foundation for wastewater treatment, and environmental applications.

4.2.1 SEM-EDS for TiO_2 /BC nanocomposites

Figure 4.3(a,b) presents the visuals that highlight the surface morphology of biochar's. A comparison of pictures (a) and (b) shows that the surface of the biochar's tended to be smooth,

with irregular-shaped particles due to the presence of various elements. Similarly, the EDS analysis (figure 4.4a,b) revealed that carbon (73.7%) and oxygen (25.9%) were the most abundant elements in the biochar samples. This suggests that biochar is mostly made of carbon, with some oxygen added. The existence of oxygen-containing functional groups (-COOH and -OH) or oxygen-containing metal minerals particles could explain the presence of oxygen. Furthermore, the analysis discovered the presence of mineral fractions like copper (0.3%) in conjunction with the biochar. The EDS layer of element particularly found in biochar is illustrated by figure 4.5 which depicts the individual EDS mapping of several elements in the prepared BC sample, including Zn, Al, O, C revealing the spatial distribution of each element in the sample. These images are generated by detecting specific X-ray lines emitted by the elements in the sample when exposed to electron bombardment in SEM.

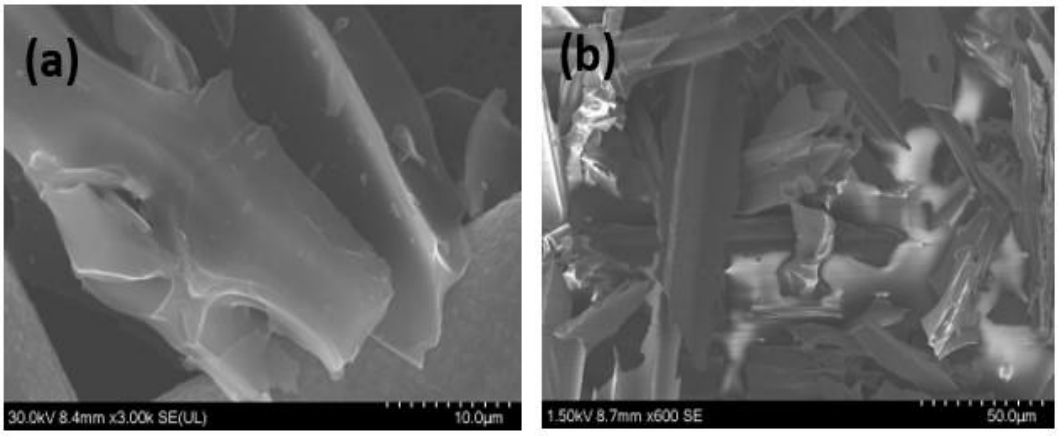

Figure 4.3: SEM image of biochar for (a) 10 µm and (b) 50 µm.

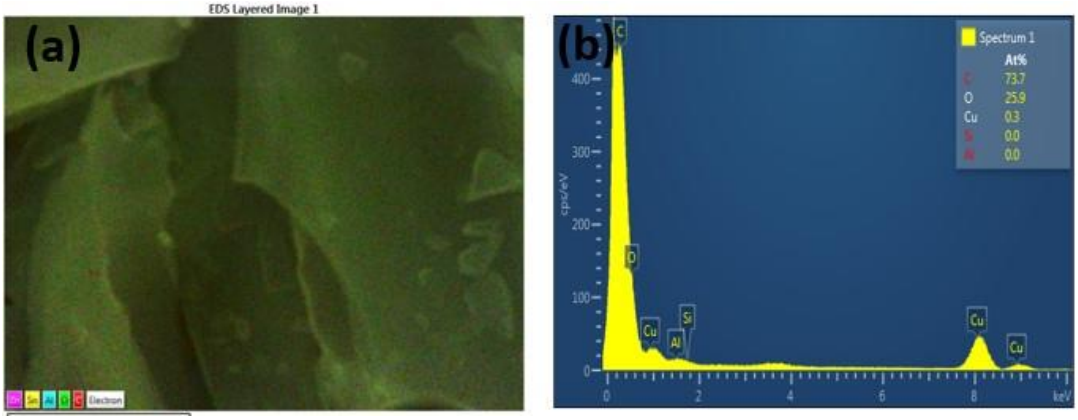

Figure 4.4: EDS image of biochar representing (a) EDS layer and (b) percentage range of the elements in the composite mass, visualized in the adequate voltage range, counted in seconds per electron-volt.

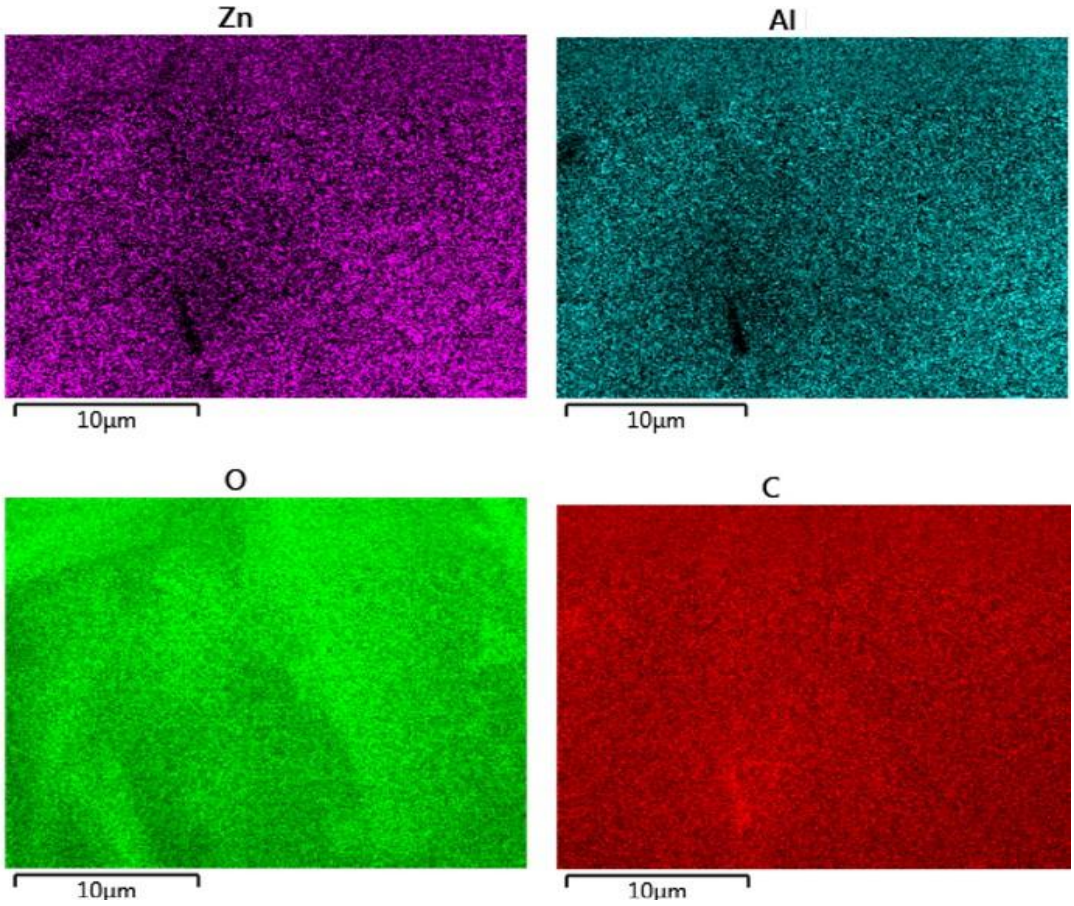

Figure 4.5: EDS layer of different elements representing Zinc (Zn), Aluminium (Al), Oxygen(O) and Carbon(C).

The SEM-EDS analysis of commercial TiO_2/BC is presented in figures 4.6(a,b) and 4.7(a,b) provide valuable insights into the elemental composition of the sample. Figures 4.7 and 4.8 show the EDS analysis of commercial TiO_2/BC, which provides vital information about the sample's elements. Mainly, the image predicts the presence of titanium (Ti), carbon (C) and oxygen (O) elements, which confirm that the sample is composed of a combination of TiO_2 and biochar. These results are significant because they provide evidence that the sample contains the desired elements.

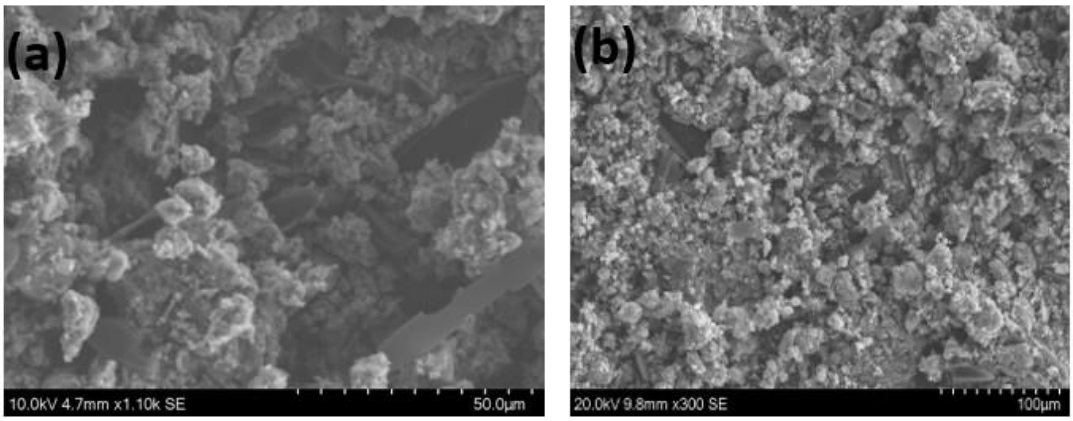

Figure 4.6:SEM images for commercial TiO_2/BC with (a) 50 µm and (b) 100 µm.

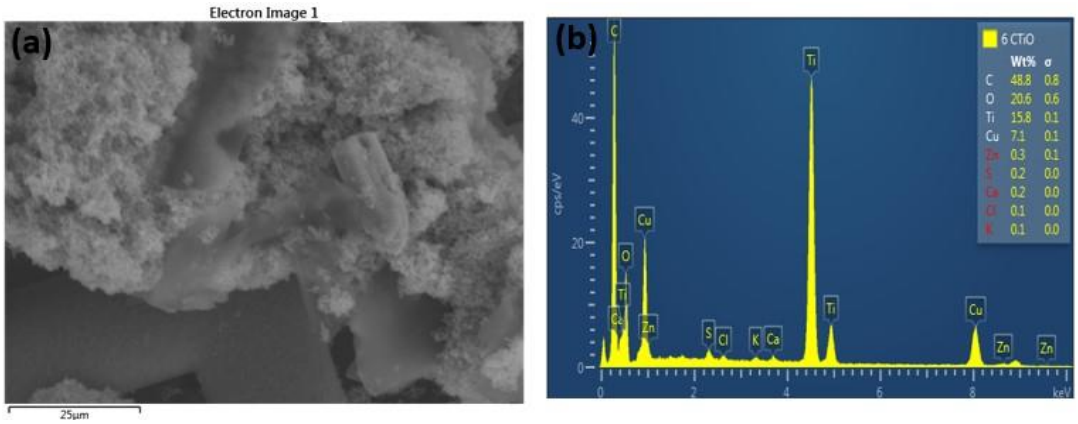

Figure 4.7:EDS images for commercial TiO_2/BC for (a) electron image and (b) percentage of elements in composite mass of TiO_2/BC sample.

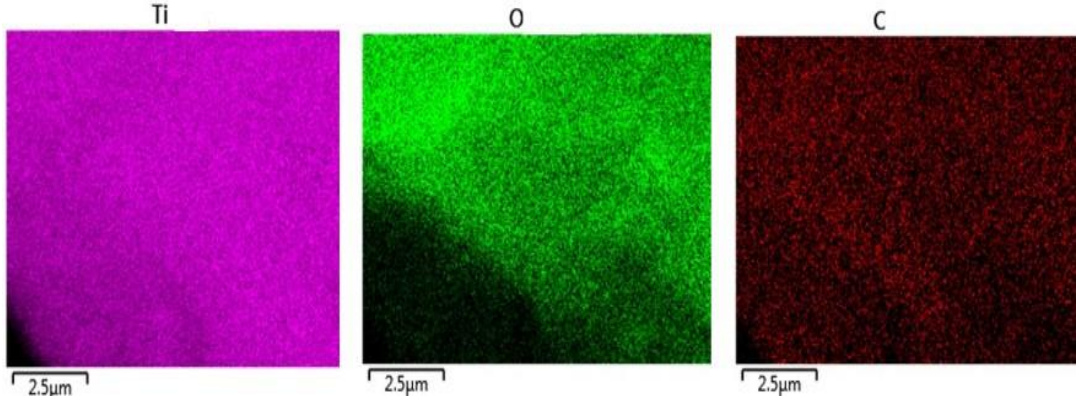

Figure 4.8: EDS mapping representing titanium (Ti), oxygen(O) and carbon(C) of commercial TiO_2/BC

Correspondingly, figures 4.9 and 4.10 show the SEM-EDS analysis for prepared TiO_2/BC respectively. This study explored the chemistry and physical structure of TiO_2/BC samples prepared for this study. Figure 4.9(a,b) showcases the physical attachment or interface between the prepared TiO_2 and biochar materials, while figure 4.10 (a,b) provides a spatial distribution of different elements in the sample through a graph of counts per second (cps) versus energy (kev) and peaks corresponding to characteristic X-rays emitted by titanium, carbon, and other elements in the sample. Figure 4.10 illustrates that prepared TiO_2/BC contains Ti, O and C with percentages of weight by 15.8, 20.6 and 48.8 respectively. EDS mapping of the sample's elements is shown in figure 4.11 and includes carbon (C), oxygen (O), and titanium (Ti).

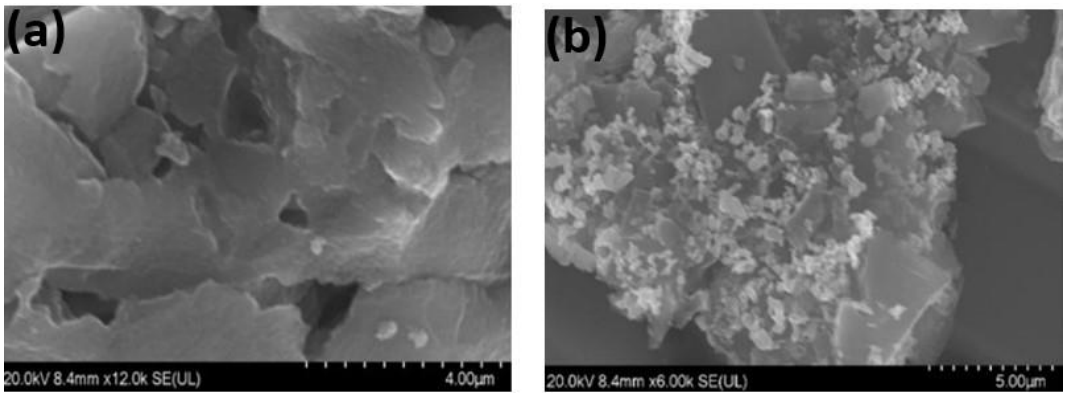

Figure 4.9:SEM images for prepared TiO_2/BC with (a) 4 µm and (b) 5µm.

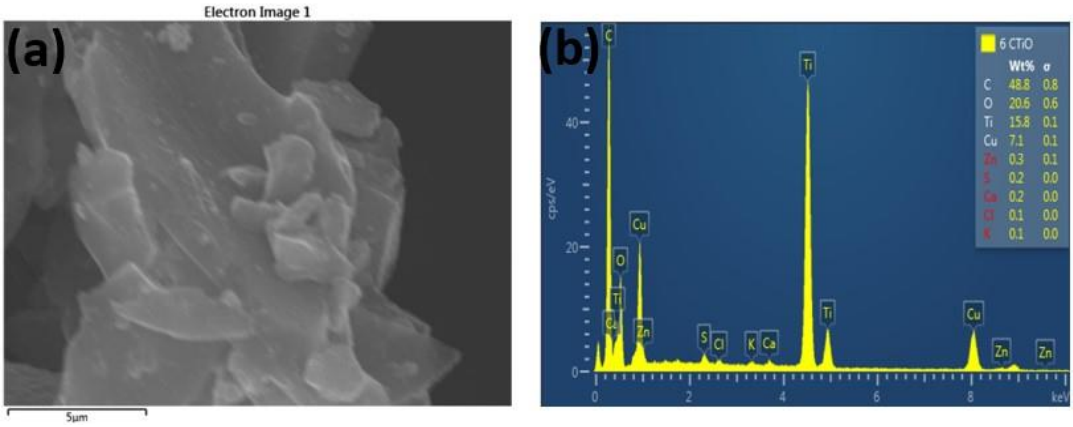

Figure 4.10:EDS images for prepared TiO_2/BC for (a) electron image and (b) percentage of elements in composite mass of TiO_2/BC sample.

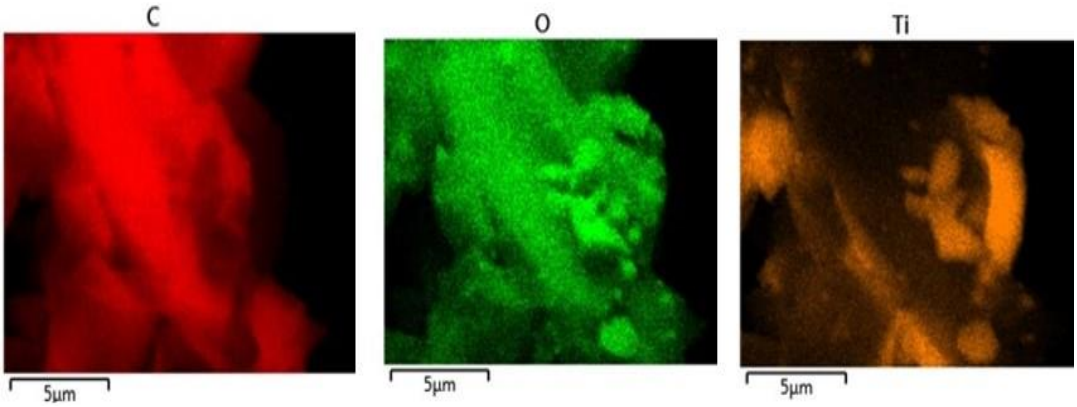

Figure 4.11:Elemental mapping of sample showing carbon(C), oxygen (O), titanium (Ti) and titanium (Ti) through EDS.

4.2.2 SEM-EDS analysis of ZnO/BC nanocomposites

Figure 4.12(a,b) showcase SEM images of commercial ZnO amalgamated with biochar at varying magnifications (10 µm and 50 µm). The former was captured at 3 kV, with a signal acquisition of 3.50 k(SE) UL, while the latter was taken at 20 kV, with a signal acquisition of 700 (SE) UL. These images serve to provide insights into the morphology and size distribution of ZnO nanoparticles, which have adhered to the biochar surface. Upon closer inspection, the presence of biochar has resulted in the clumping and agglomeration of the ZnO particles in the composite catalysts, leading to the formation of larger particles. The image in figure 4.12(b) depicts the structure of composite catalysts, specifically the pores within them. The image shows that the pore structure is irregular rather than smooth and equal. This variation is caused by two major variables. First, the inner walls of the biochar break down during pyrolysis, a high-temperature process [69] and second, the pores of the biochar get obstructed or filled with material that falls into them during pyrolysis. These exciting findings show that biochar has a significant impact on the structure and performance of ZnO-based catalysts.

The EDX analysis of figure 4.13(a,b) showed that the commercial ZnO/BC is predominantly composed of carbon and oxygen, with some amount of zinc present. The atomic percentages of each element were 69.8% for carbon, 29.5% for oxygen, and 0.7% for zinc. Specifically, the data suggests that the sample is likely a composite material consisting of biochar and ZnO

nanoparticles. Similarly, figure 4.14 shows the mapping of element present in prepared zinc oxide biochar which shows the distribution of each element in the sample.

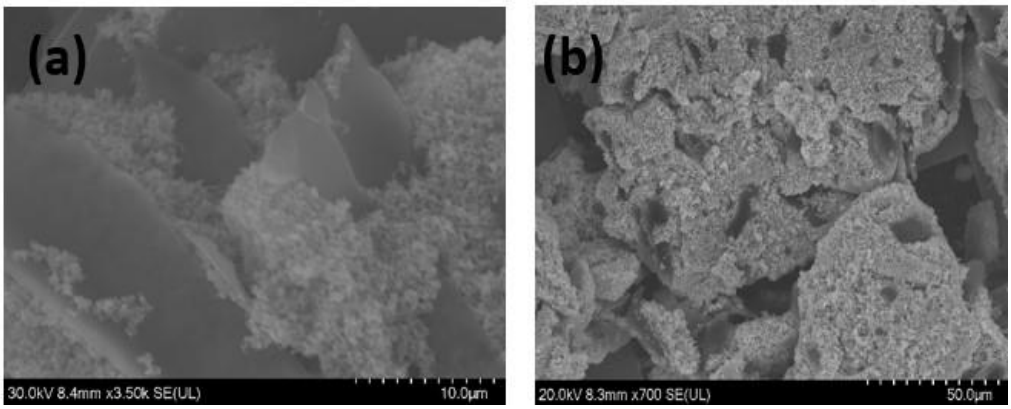

Figure 4.12:SEM images for commercial ZnO/BC sample with (a) 10 µm and (b) 50µm

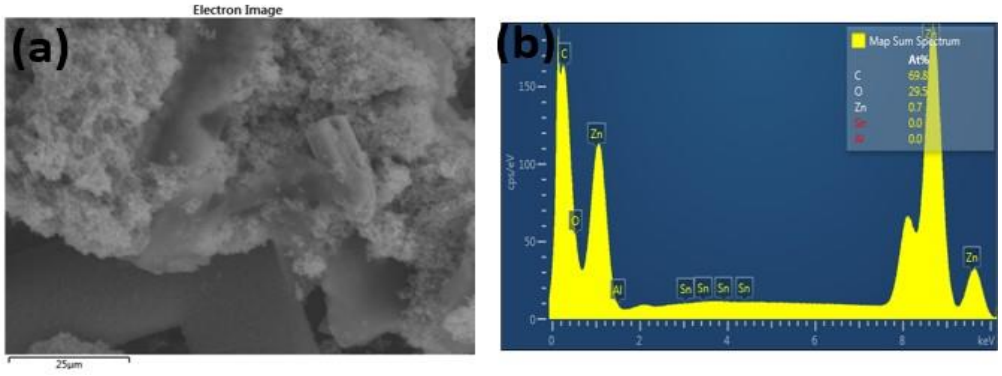

Figure 4.13:EDS images for commercial ZnO/BC sample (a) electron image and (b) percentage of elements in composite mass.

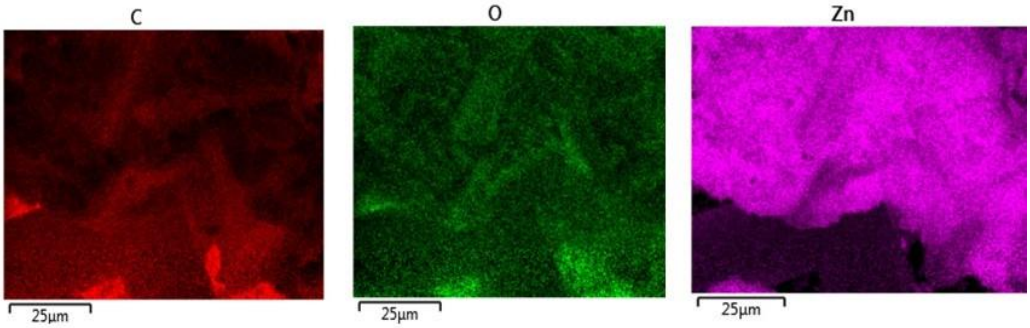

Figure 4.14:Elemental mapping for commercial ZnO/BC sample representing carbon (C), oxygen (O) and zinc (Zn).

SEM analysis was conducted to study the morphology of prepared ZnO/BC, as depicted in figure 4.15 (a,b). The results showed that ZnO particles exhibited a cluster structure, likely due to the autoclave treatment with BC under high pressure in a Lenton chamber. A portion of the cluster structure was found to be adhered to the BC. To further demonstrate the synthesis of the ZnO/BC NPs, an EDS image was obtained (figure 4.16a,b) and the corresponding EDS mapping of elements of Zn, O, and C are displayed in Figure 4.17. Figure 4.16 b revealed that the sample had the highest percentage of carbon, followed by oxygen and zinc. This finding suggested that ZnO was uniformly dispersed on the surface of BC. Additionally, the presence of ZnO was confirmed by the element distribution analysis.

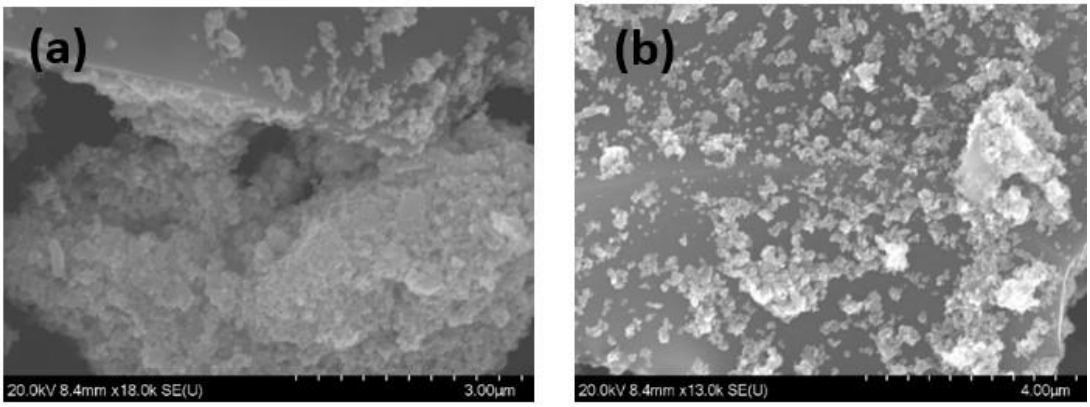

Figure 4.15:SEM images for prepared ZnO/BC with (a) 3 µm and (b) 4 µm

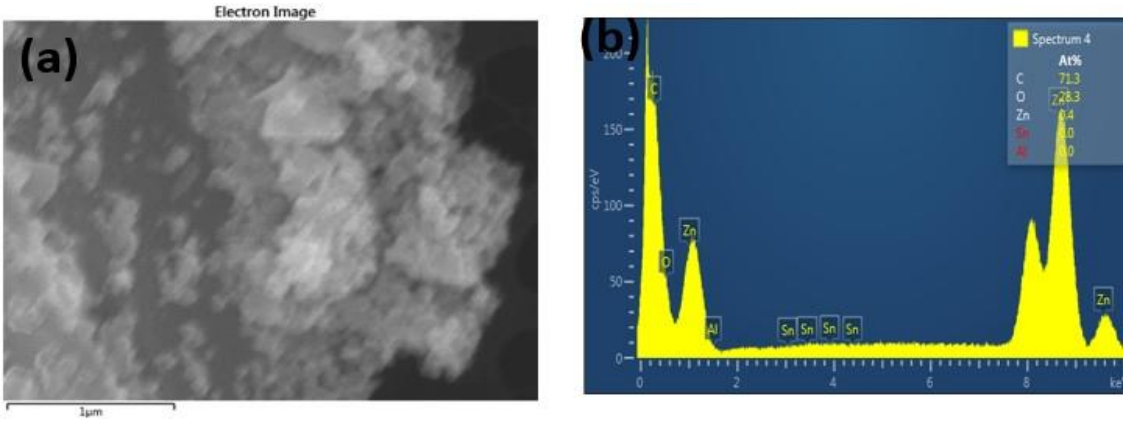

Figure 4.16: EDS images for prepared ZnO/BC sample (a) electron image and (b) percentage of elements in composite mass of ZnO/BC sample.

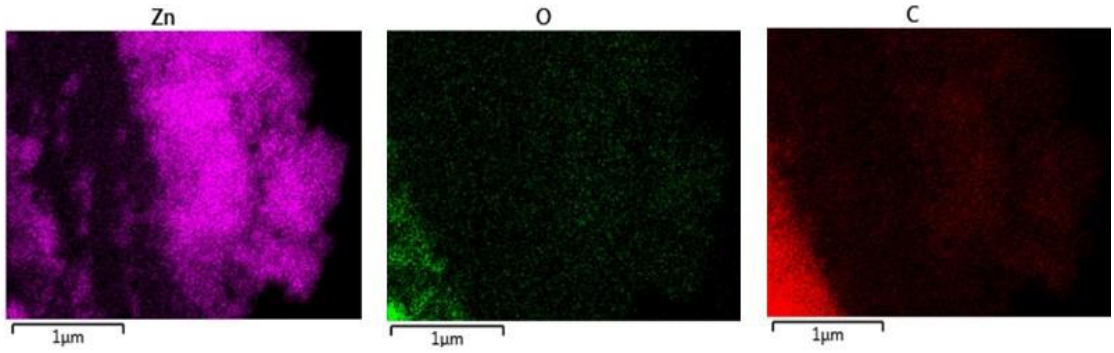

Figure 4.17:Elemental mapping for prepared ZnO/BC representing zinc (Zn), carbon(C) and oxygen (O).

4.3 FTIR analysis of TiO_2, ZnO and biochar TiO_2, ZnO composites

The FTIR spectra obtained for biochar and its composite with TiO_2 and ZnO, as shown in figure 4.18 a, appear to have a similar pattern to the spectra obtained for biochar and its composite with prepared TiO_2 and ZnO, as presented in figure 4.18b. The primary objective of the FTIR analysis was to identify the functional groups present on the sample surfaces. The results showed that the peak at 1,634 cm^{-1}, attributed to the C–C atoms, was present in all carbon-based samples (BC, BC/TiO_2 and BC/ZnO) while vibrations between 3,475 and 3,450 cm^{-1}, attributed to O–H bond vibrations, were identified in all the samples [69]. The characteristic peaks at 3423 cm^{-1}, which corresponds to -OH stretching vibration peaks, were observed in BC, TiO_2, and BC/TiO_2 which also have similar result shown by research paper [70]. However, the intensity of this peak was found to be weakened in the prepared composite material, indicating a reduction in the surface hydroxyl group content of the biochar after it was loaded with TiO_2. This effect is believed to result from a fracture association reaction between the surface hydroxyl group and TiO_2. Furthermore, the characteristic peak at 1652 cm^{-1}, corresponding to the C=O bond stretching vibration [70], was also observed. On the other hand, Ti-O bond in TiO_2 and its composites determines structural properties of material and phases [71] and plays a critical role in anchoring the TiO_2 nanoparticles onto the biochar surface, thereby improving its stability and durability. This bonding also facilitates the transfer of photo-generated electrons from the TiO_2 nanoparticles to the biochar, resulting in enhanced photocatalytic properties. As a result, the Ti-O bond is a crucial component of the TiO_2 biochar photocatalyst,

which shows significant potential for environmental remediation. In addition, the study included UV-Vis Spectrophotometer analysis of TiO_2 and ZnO nanoparticles with their composites with biochar.

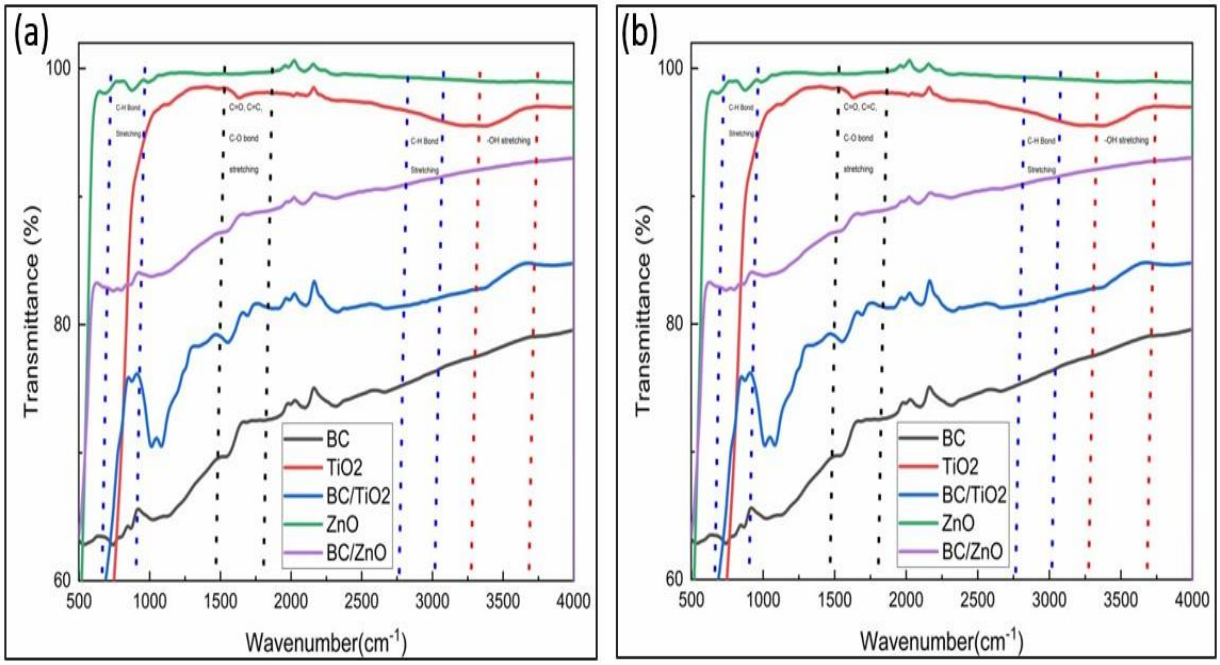

Figure 4.18:FTIR analysis for (a) commercial samples and (b) prepared samples

4.4 Photocatalytic degradation

4.4.1 Kinetic analysis of pure MO

The purpose of this research was to conduct a kinetic analysis on a pure MO solution and validate the application of the Beer-Lambert law by establishing a link between absorbance and concentration. For this study, various and different concentration of MO solution (2 ppm, 4 ppm, 6 ppm, 8 ppm, 10 ppm, 12 ppm, 14 ppm, 16 ppm,18 ppm and 20ppm, respectively) were prepared as shown in figure 4.19 to confirm that the absorbance of the MO solution used in this experiment obeys the Beer-Lambert law.

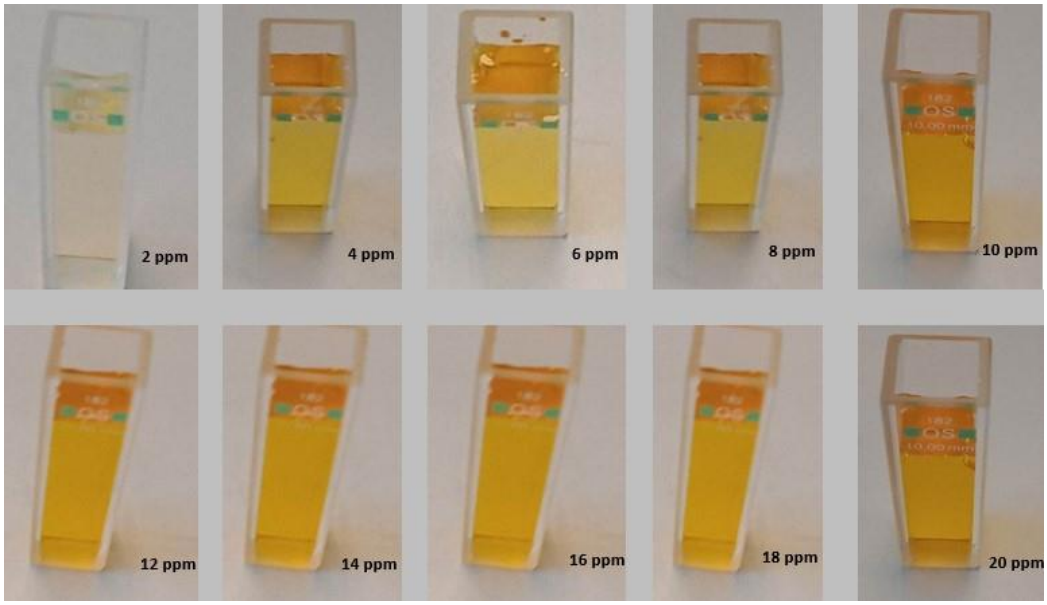

Figure 4.19:Photograph view of MO solution in cuvettes

As concentration increases, the MO solution turns a darker orange color. Figure 4.20 shows the results of monitoring their UV-Vis absorption spectra. The absorbance values at 464nm for each concentration of MO solutions was plotted against their respective concentrations, resulting in a straight line that passes through the origin, as demonstrated in figure 4.21. This line represents a strong linear correlation between the concentration and absorbance of MO solutions within the 2-20 ppm concentration range.

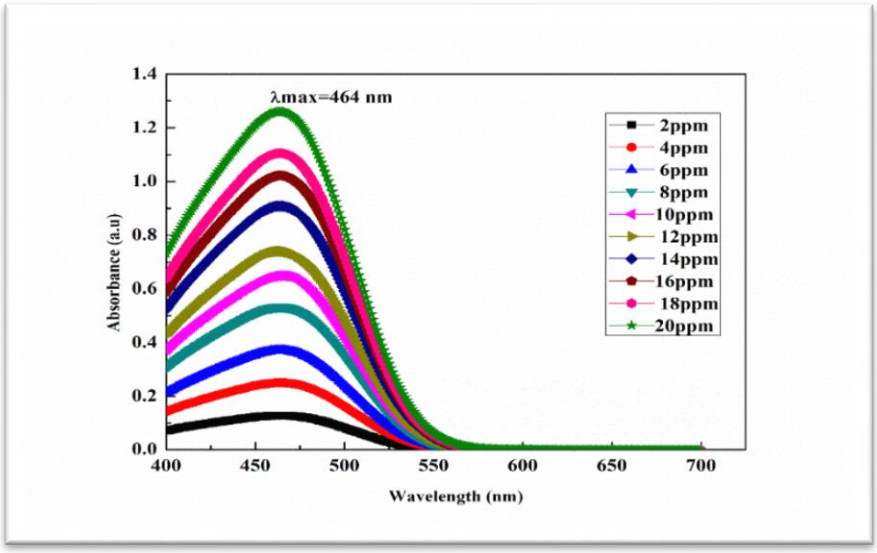

Figure 4.20:Absorbance of MO solutions versus their concentrations., calibration curve for MO solution concentrations

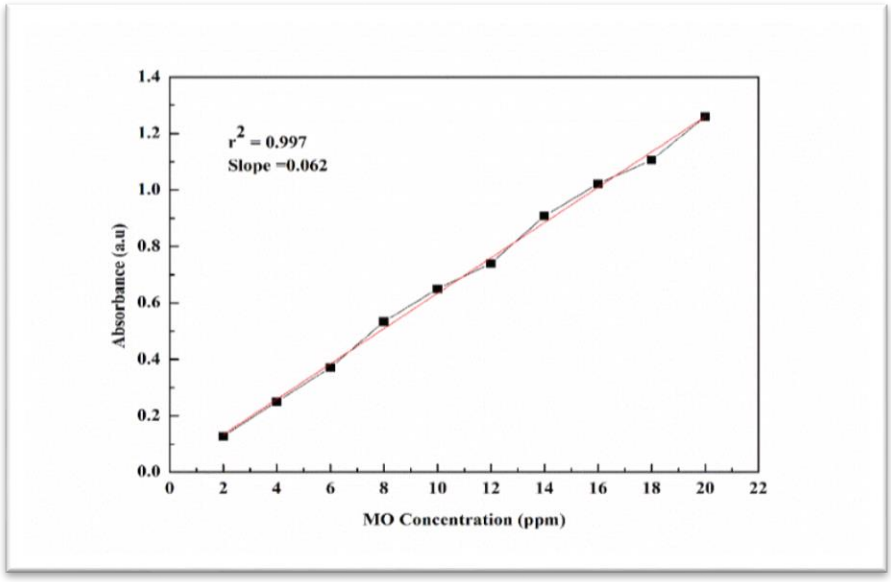

Figure 4.21:Absorbance of MO solutions versus their concentrations., calibration curve for MO solution concentrations.

The linear relationship revealed in the plot adds to the data, confirming the accuracy of equation 3.11 and its ability to estimate the percentage deterioration based on absorbance and concentration values.

4.4.2 Photodegradation of MO under TiO_2, ZnO, TiO_2/BC and ZnO/BC composites

The photocatalytic activity of TiO_2 and ZnO catalysts was assessed using methyl orange as the model pollutant in experiments conducted in a 100 mL Pyrex glass container under the radiation of a tungsten halogen light source (260 nm - 2500 nm, 600 W, NBeT, China), which is available at the USN laboratory. For TiO_2 nano particles, solutions containing 75 mg of the catalysts were prepared in 75 mL of methyl orange solution (20 ppm stock solution) and the experiments were carried out under gentle radiance of the tungsten halogen light as solar light source. Absorption spectra of methyl orange degradation catalyzed by commercial TiO_2, commercial TiO_2 biochar, prepared TiO_2, and prepared TiO_2-biochar were obtained and analyzed using a high-performance spectrophotometer to provide insights into the catalytic efficiency of these materials and their potential for the degradation of organic pollutants.

Similarly, for ZnO nano particles, solutions containing 75 mg of the catalyst were prepared in 75 mL of methyl orange solution (20 ppm stock solution) and the degradation of methyl orange was monitored over time under the exposure of a tungsten halogen light source, following a similar procedure as that used for TiO_2. The same quantity of catalyst and methyl orange solution was used for commercial ZnO, prepared ZnO, commercial ZnO-biochar and prepared Zno-biochar to ensure consistency in the experiments. The resulting absorption spectra of methyl orange under the catalysis of ZnO nano particles were analyzed to provide valuable information on the effectiveness of ZnO and its composite in the degradation of organic pollutants. All experimental details were conducted according to standard procedures and protocols, and rigorous measurements were recorded and analyzed to ensure accuracy and reliability of the results. Figures 4.22 and 4.23 show how the absorption spectra of methyl orange are affected by various materials like TiO_2, and ZnO nanoparticles, revealing the captivating interplay of light and matter. The degradation of MO under solar irradiation utilizing various photocatalysts, including commercial TiO_2, commercial TiO_2 with BC, prepared TiO_2, and prepared TiO_2 with BC was investigated. The degradation process is depicted in figure 4.22, with the curves (a), (b), (c), and (d) reflecting the various photocatalysts. Curves (a), (b), and (d) showed complete MO degradation in 180 minutes, indicating the high efficiency of commercial TiO_2, commercial TiO_2 with BC, and prepared TiO_2 with BC in degrading MO. The deterioration rate of curve (c) corresponding to the prepared TiO_2 photocatalyst, on the other hand, was slower. MO was entirely degraded in 240 minutes, implying that this photocatalyst necessitates a longer exposure duration.

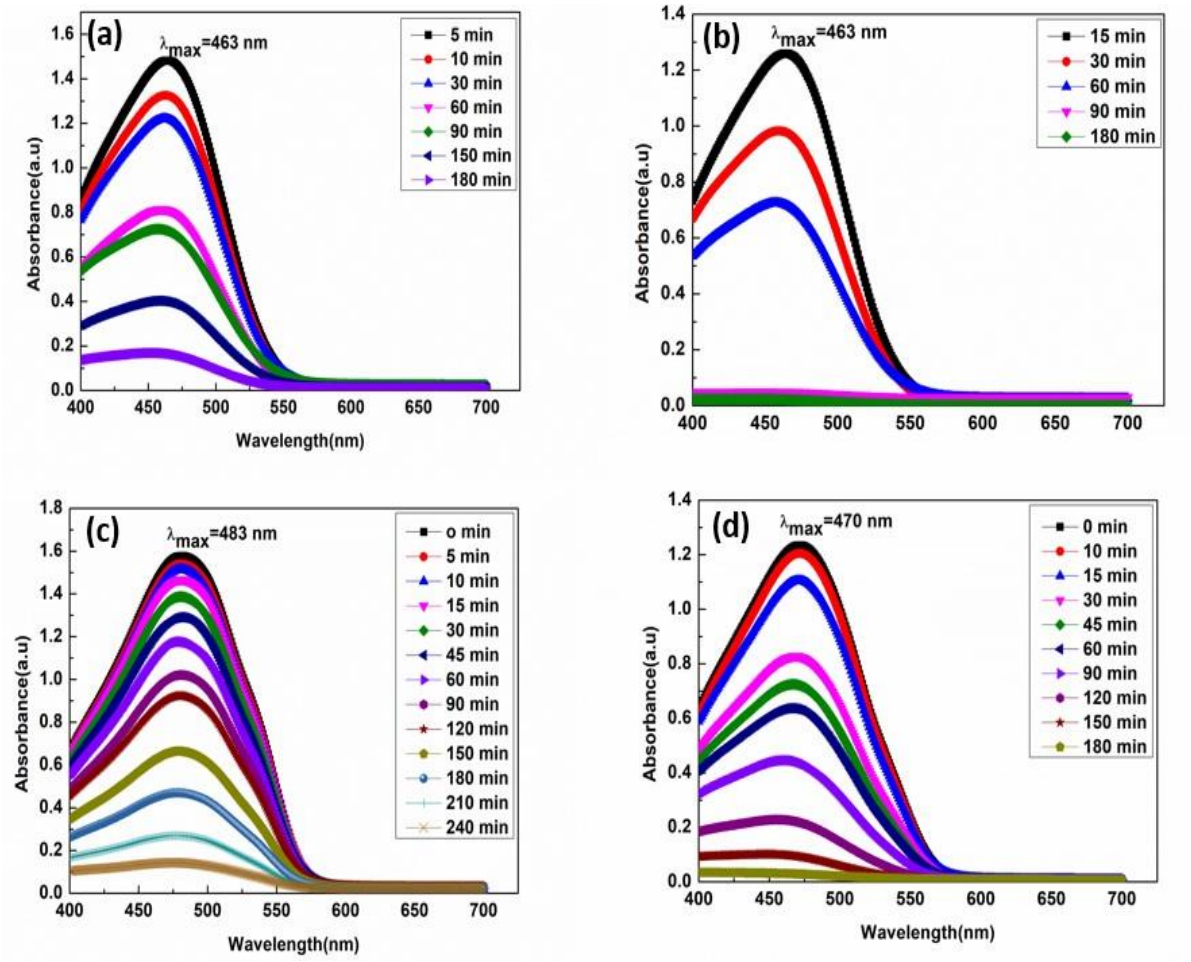

Figure 4.22:Degradation of MO under tungsten halogen lamp in presence of (a) commercial TiO_2, (b) commercial TiO_2/BC (c) prepared TiO_2 and (d) prepared TiO_2/BC.

Similar results were obtained when MO was degraded in the presence of ZnO. Figure 4.23(c) shows that while employing prepared ZnO, the degradation process took a lengthy time compared to other catalysts such as commercial ZnO, commercial ZnO with BC, and prepared ZnO with BC, which are represented by samples marked as a, b, and d, respectively.

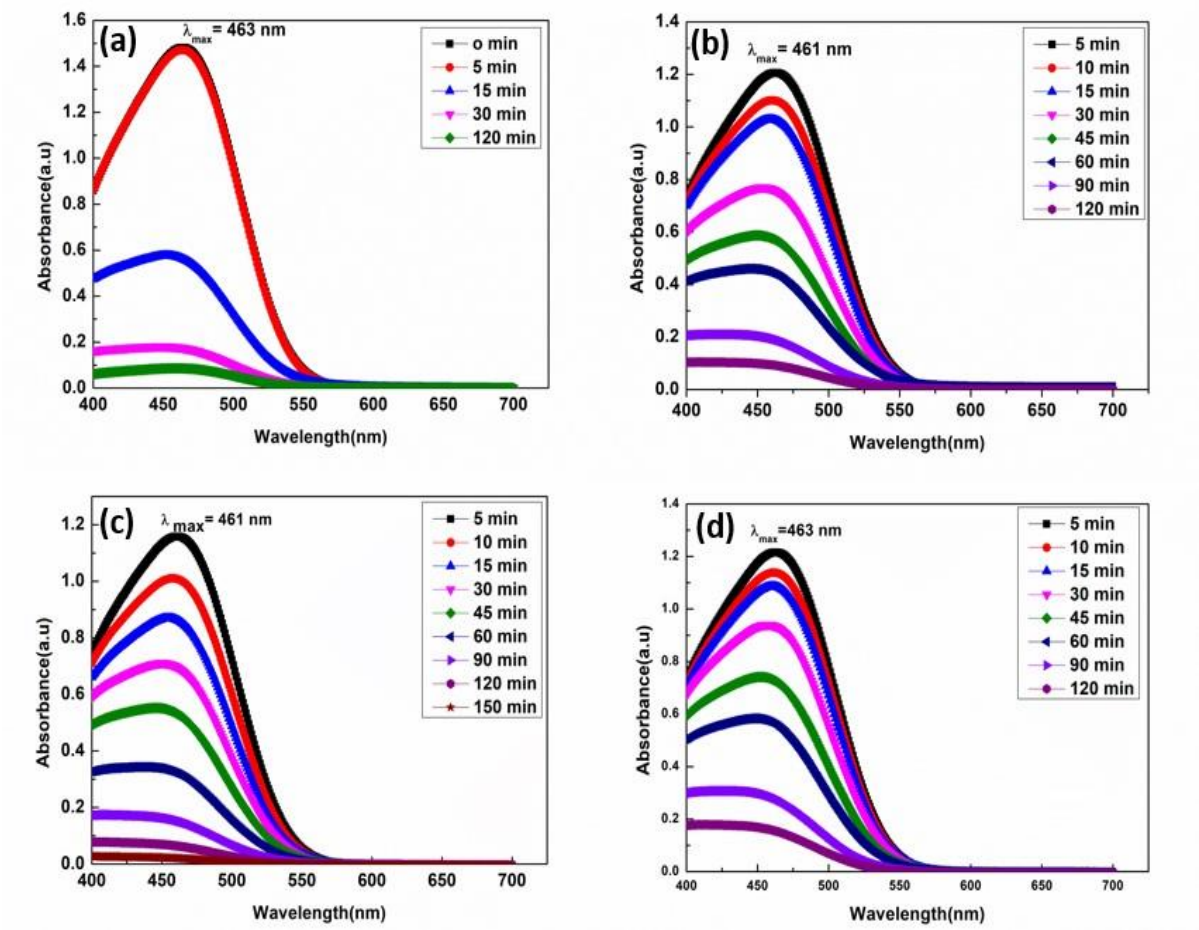

Figure 4.23:Degradation of MO under solar light in presence of (a) commercial ZnO, (b) commercial ZnO/BC, (c) prepared ZnO and (d) prepared ZnO/BC.

In figure 4.24 of the research study, two plots are presented. Figure 4.24 (a) depicts the dynamic behavior of absorbance (A/A_0) over time for TiO_2 particles and their composites, providing insights into the changes in relative absorbance concerning the initial absorbance (A_0) in the TiO_2 system. In figure 4.24 (b), a plot of concentration (C) relative to the initial concentration (C_o) is presented for TiO_2 nanoparticles and composites. Similarly, in figure 4.25, there are two plots as well. Figure 4.25 (a) represents the relative absorbance (A/A_0) for ZnO nanoparticles and their composites, while figure 4.25 (b) shows the concentration (C) relative to the initial concentration (C_0) for ZnO and its composites. These plots serve as crucial visual aids, providing valuable information about the absorbance and concentration dynamics in the respective systems.

Under dark conditions, when BC is combined with commercial TiO_2 or prepared TiO_2, the concentration of MO does not change significantly as shown by figure 4.24(a,b). This indicates that the combination of BC with either commercial or prepared TiO_2 does not lead to noticeable degradation of MO under dark conditions. However, when the same combinations of BC with commercial or prepared TiO_2 are exposed to light, the degradation of MO becomes evident after 60 min dark. The concentration of MO decreases with time, suggesting that the presence of light enhances the degradation process when BC and TiO_2 catalysts are used together. In figure 4.24a, the degradation of MO is seen to properly after 15 minutes of solar irradiation for all photocatalysts. At the time, the relative absorbance values for commercial TiO_2, commercial TiO_2 with BC, prepared TiO_2, and prepared TiO_2 with BC were 0.86, 0.92, 0.88, and 0.90, respectively. Figure 4.24b shows a similar nature and identical relative concentration value at 15 minutes. The exactness in number is due to the linear relationship between absorption and concentration values, as shown in figure 4.21. Moving on to figure 4.25(a,b), a similar trend is observed which reveals that the relative absorbance value for commercial ZnO, commercial ZnO with BC, prepared ZnO and prepared ZnO with BC found to be same. The relative absorbance and concentration values for 15 min for commercial ZnO, commercial ZnO with BC, prepared ZnO and prepared ZnO with BC are 0.30, 0.87, 0.78, and 0.88 respectively.

This indicates that the TiO_2 and ZnO both catalysts alone are effective in degrading MO under the influence of light. Also, we noticed from the figure 4.24 and 4.25, that that the presence of only BC does not contribute to the degradation of MO in the presence of light, regardless of the type of TiO_2 and ZnO catalyst used. The plot reveals that the relative absorbance of more than 1.0 can be noticed in case of BC after 30 min in both figure 4.24 and 4.25. These results emphasize the crucial role of BC, TiO_2 and ZnO catalysts in the degradation of MO, as well as the importance of light as an external factor in facilitating the degradation process. Further analysis and investigation are needed to better understand the underlying mechanisms and optimize the degradation efficiency of MO under these conditions.

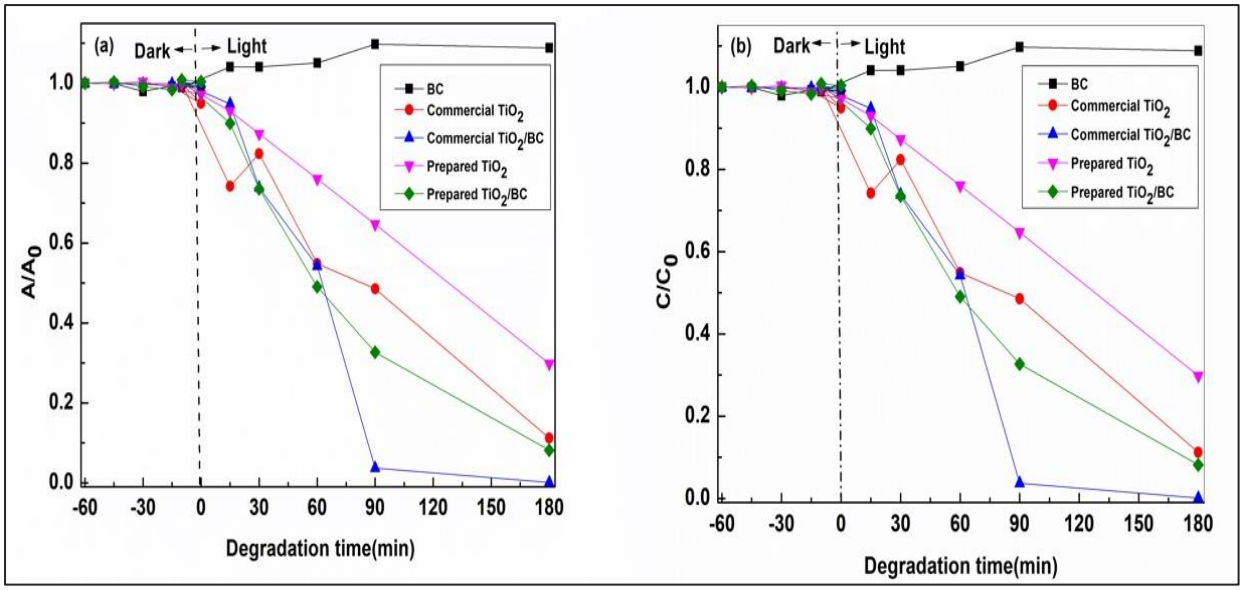

Figure 4.24:Comparative analysis of (a) relative absorbance (A/A_0) and (b) relative concentration (C/C_0) for TiO_2 nano particles and their composites.

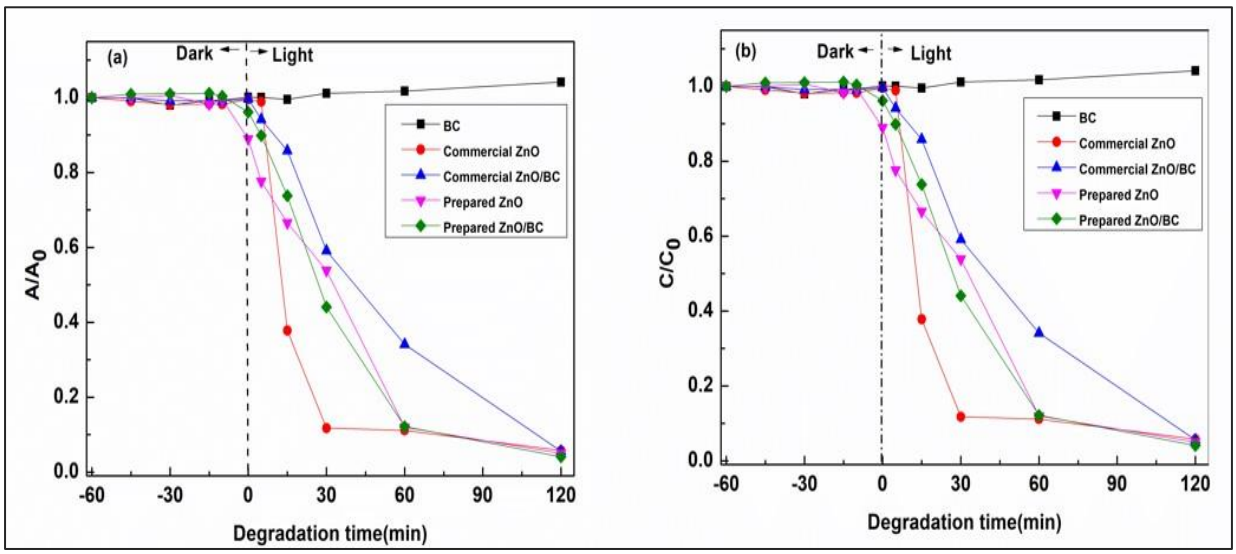

Figure 4.25:Comparative analysis of (a) relative absorbance (A/Ao) and (b) relative concentration (C/Co) for ZnO nano particles and their composites.

4.4.3 Photocatalytic degradation efficiency for TiO_2 and ZnO nano particles

Methyl orange, a widely used azo dye, was selected as the target compound to investigate the photocatalytic degradation efficiency of titanium dioxide (TiO_2) and zinc oxide (ZnO) nanoparticles. The degradation efficiency was calculated using the formula,

% Degradation = $(C_0 - C_t) / C_0 \times 100$ % (from equation 3.11)

Where, C_0 represents the initial concentration of methyl orange before light irradiation, and C_t represents the concentration of methyl orange at a specific time during or after light irradiation.

Figure 4.26(a,b) illustrates the comparative degradation efficiency of methyl orange (MO) under various conditions, including the presence of commercial TiO_2, prepared TiO_2, commercial ZnO, and prepared ZnO catalysts, with a specific focus on evaluating the impact of biochar as an additional factor. Notably, the results obtained from the study revealed that the degradation of MO under TiO_2 and ZnO catalysts was lower in comparison to the degradation achieved when biochar was added to the system. Figure 4.26a showed a remarkable increase in the degradation of methyl orange under TiO_2/BC of 90%. Degradation of roughly 60% is reported in prepared TiO_2, while degradation of 70% is observed in commercial TiO_2 as depicted in figure 4.26a. Similarly, 4.26 b reveals the degradation efficiency of MO under commercial ZnO, prepared ZnO and prepared ZnO with BC was found to be 80%, and for commercial ZnO with BC was found to be 90%. Thus, figure 4.26(a,b) showed a remarkable increase in the degradation of methyl orange under TiO_2/BC and ZnO/BC, surpassing the 90% threshold, which is a significant achievement in the field of photocatalysis. Lu et al. (2019) [17], which has demonstrated the potential of these composites in environmental remediation, and their results strongly support this observation. The findings of this study provide valuable insights into the progress of advanced photocatalytic materials and their potential applications in sustainable environmental applications. The degradation of MO occurred in the presence of biochar without adding any other catalyst. This investigation suggests that biochar may lack the required mechanisms or catalytic characteristics to enhance MO breakdown. As a result, additional components or catalytic agents are required to accomplish considerable MO degradation in such systems.

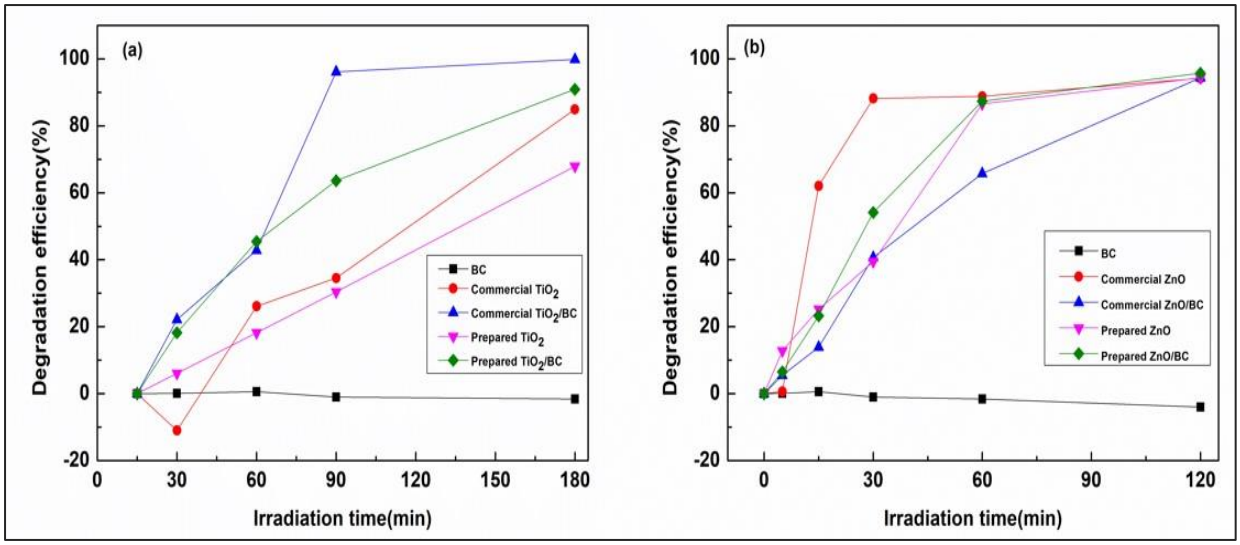

Figure 4.26:Methyl Orange degradation efficiency verses plot under (a)TiO_2 nano particles (b) ZnO nano particles and their composites.

4.4.4 Kinetic analysis of photocatalytic process

Based on the results obtained, the first-order kinetic model was selected as the most suitable approach for describing the degradation kinetics of MO. This choice was primarily driven by the high degree of fit exhibited by the first-order model, as demonstrated by the r^2 values. Additionally, the observed trend of degradation rates further supported the validity of the first-order kinetic model in capturing the behaviour of the degradation process.

A plot of $\ln(C_0/C_t)$ versus degradation time (t) for the photocatalytic experiments using TiO_2, biochar-TiO_2 composites and ZnO, biochar-ZnO composites on MO degradation process is shown in figures 4.27 and 4.28, respectively. The values of the pseudo-first-order rate constant (k) can be estimated by regression analysis of the linear curve in the plot. The calculated k values and the correlation coefficients (r^2), which indicates the degree of agreement of the process in accordance with the kinetic model, are presented in the Table 4.1. Analyzing the plot of ln (Co/Ct) versus time reveals that the effectiveness of MO degradation varies greatly depending on the type of photocatalyst used. A moderate relationship between degradation rates and time is demonstrated by the correlation coefficient ($r^2 = 0.9477$) for commercial TiO_2. On the other hand, the other three photocatalysts had substantially stronger correlations with higher r^2 values. The degrading procedure produced a stronger correlation coefficient of r^2 =

0.9582 for commercial TiO_2/BC nanocomposites (figure4.27b). When compared to commercial TiO_2, this indicates improved degrading efficiency. There was a significant improvement in MO degradation with the prepared TiO_2 (figure 4.27 c) having a better correlation and r^2 value of 0.9776. As expected, the highest correlation coefficient was found for prepared TiO_2/BC nanocomposites (figure 4.27d). Furthermore, the almost linear plot observed in figure d also suggests a consistent and efficient degradation of MO under these photocatalyst.

Also, on analyzing the ln (Co/Ct) versus time plots, it becomes evident that the photocatalytic degradation efficiency of MO varies among the different photocatalysts. For commercial ZnO (figure4.28a), a correlation coefficient of r^2 = 0.7555 is observed, suggesting a substantial association between the degradation rates and time. Interestingly, the prepared ZnO (figure 4.28c) exhibits even better MO degradation, as indicated by the slightly higher correlation coefficient of r^2 = 0.9524. This finding implies an enhanced photocatalytic activity of prepared ZnO compared to its commercial counterpart, thus rendering it more effective in degrading MO. Contrary to the trend observed with ZnO, the commercial ZnO/BC nano composites (figure4.28 b) demonstrated superior degradation performance compared to the prepared ZnO/BC nano composites. This is evidenced by the higher correlation coefficient value of r^2 = 0.9828 obtained for the commercial ZnO/BC, whereas the prepared ZnO/BC nanocomposites exhibited a slightly lower correlation coefficient of r^2 = 0.9728. Below figure 4.27 and 4.28 depicts pseudo first order kinetic analysis of MO under TiO_2, ZnO with their composites with biochar.

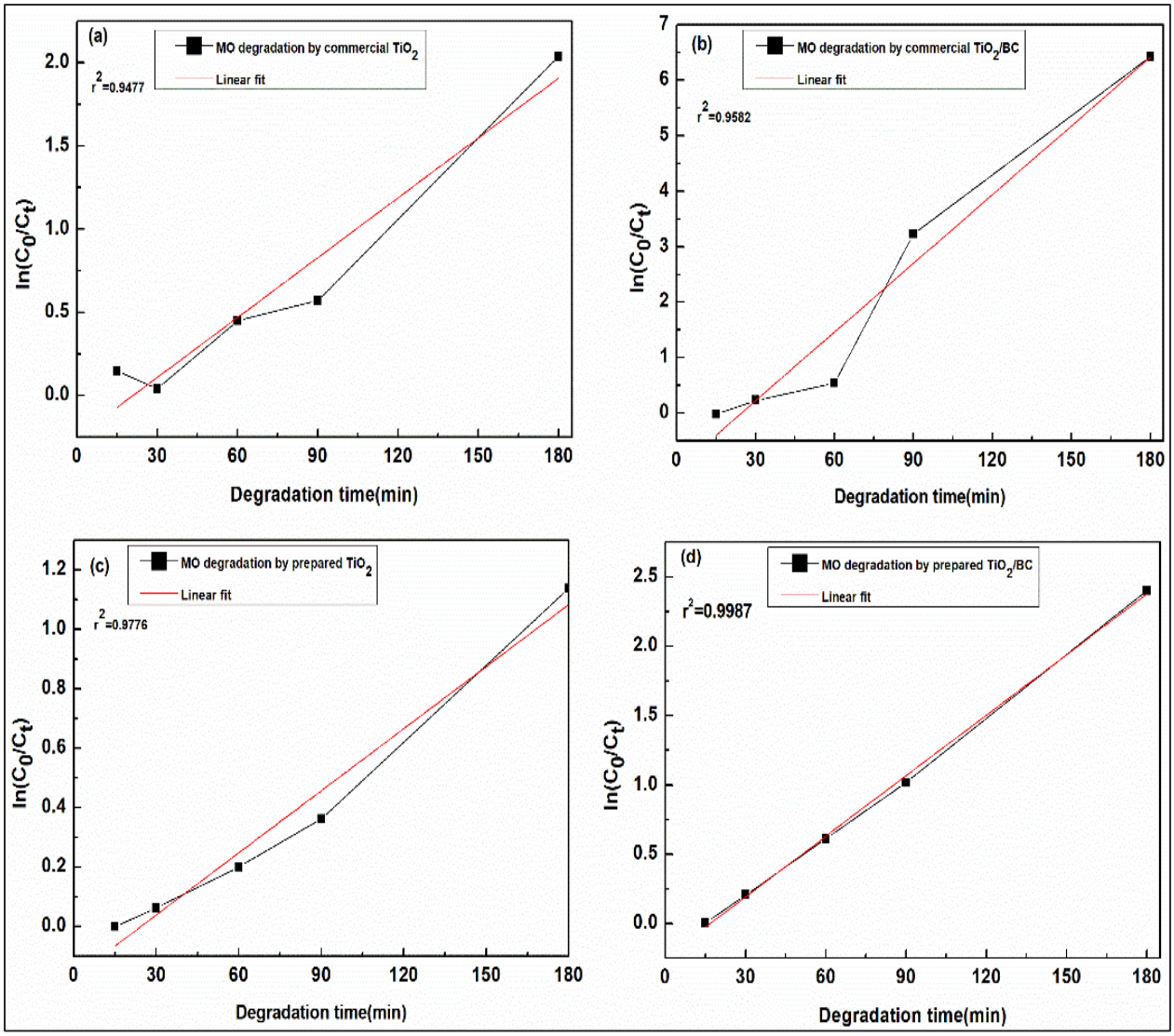

Figure 4.27: Pseudo first order kinetic analysis for degradation of MO under solar light using as photocatalyst (a) commercial TiO_2 (b) commercial TiO_2/ BC, (c) prepared TiO_2 and (d) prepared TiO_2/ BC.

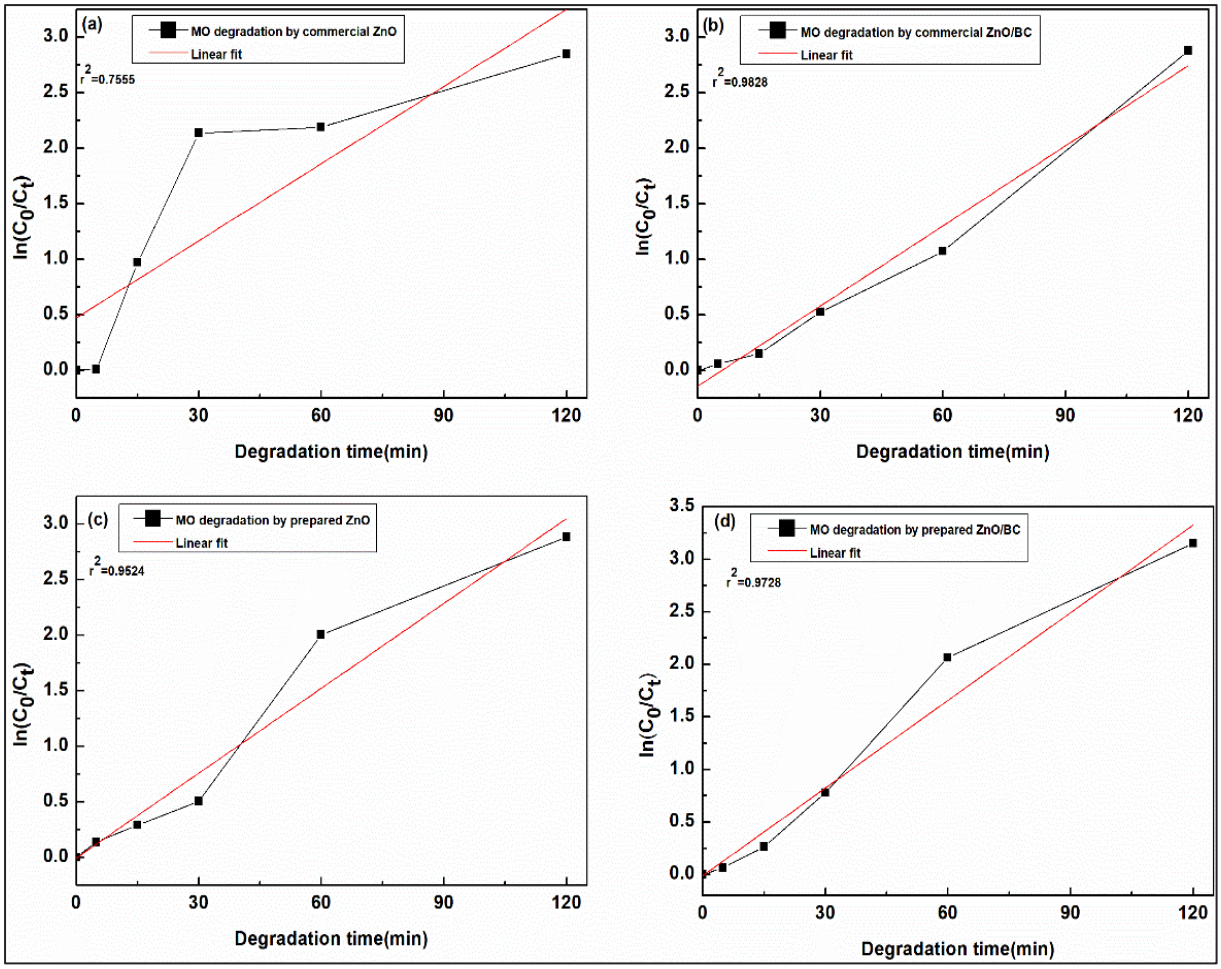

Figure 4.28:First order kinetic analysis for degradation of MO under solar light using as photocatalyst (a) commercial ZnO (b) commercial ZnO/ BC, (c) prepared ZnO and (d) prepared ZnO /BC.

Table 4.1: Results from fitting of photocatalytic kinetic of MO

Catalyst	k(min^{-1})	r^2
Commercial TiO_2	0.0119	0.9477
Commercial TiO_2 /BC	0.0412	0.9582
Prepared TiO_2	0.0069	0.9776
Prepared TiO_2/ BC	0.0175	0.9987
Commercial ZnO	0.0231	0.7555
Commercial ZnO/BC	0.0241	0.9828
Prepared ZnO	0.0254	0.9524
Prepared ZnO /BC	0.0278	0.9728

The column plot figure 4.29(a,b) shows that when biochar is combined with titanium dioxide (TiO_2) or zinc oxide (ZnO), the degradation of methyl orange (MO) is enhanced. Specifically, "commercial TiO_2 biochar" and "prepared TiO_2 biochar" have higher MO degradation rates with values 0.0412min^{-1} and 0.0175min^{-1} respectively compared to "commercial TiO_2" and "prepared TiO_2" whose values are 0.0119 min^{-1} and 0.0069 min^{-1} respectively. Similarly, "commercial ZnO biochar" and "prepared ZnO biochar" has degradation rate for MO as 0.0241 min^{-1} and 0.0278 min^{-1} respectively exhibit slightly higher MO degradation rates compared to "commercial ZnO" and "prepared ZnO" with values as 0.0231 and 0.0254 respectively. These findings suggest that biochar may boost the effectiveness of TiO_2 and ZnO in degrading MO. This claim is supported by research work done by N.P.F. Gonçalves et al [70].

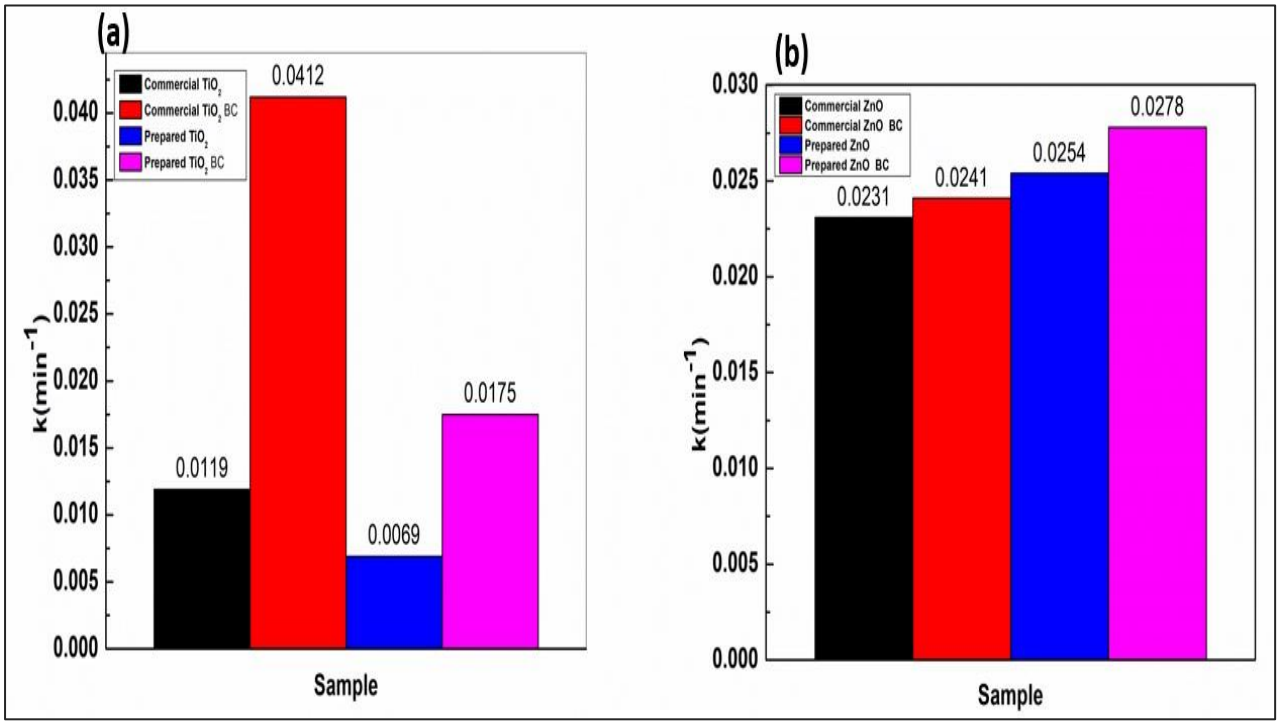

Figure 4.29:Degradation rate of MO under solar light as photocatalyst (a) commercial TiO_2, commercial TiO_2 /BC, prepared TiO_2 and prepared TiO_2 /BC and (b) commercial ZnO, commercial ZnO/ BC, prepared ZnO and prepared ZnO/ BC.

The pseudo-second-order kinetic model was also applied for all photocatalytic reactions (figure 4.30 and 4.31) by plotting t/q_t versus degradation time (t), which gives q_e equal to 1/slope and

K equal to slope^2/intercept. Kinetic parameters on the MO photodegradation under solar light using the previously discussed composites are given in Table 4.2. The correlation coefficient (r^2) values diverged significantly from unity (1.0) after careful inspection of the r^2 values and linear fit line as shown in figures (4.30 and 4.31). This deviation from a perfect match indicates that the experimental data did not fit the pseudo-second order kinetic model well. These findings imply that our experimental settings and corresponding catalyst systems failed to meet the assumptions and expectations of the pseudo-second order kinetic model. The calculated value of second order kinetic parameters of the adsorption of methyl orange on nano particles and its composites is shown in table 4.2.

For the commercial TiO_2 samples, an r^2 value of 0.6949 was obtained, indicating a moderate degree of correspondence (approximately 69.49% alignment). Similarly, the commercial TiO_2/BC nanocomposites displayed an r^2 value of 0.8188 (around 81.88% agreement). Regarding the prepared TiO_2 samples, the r^2 value yielded 0.4100, denoting a relatively weaker association. However, for the prepared TiO_2/BC nanocomposites, a higher r^2 value of 0.8446 was observed, indicating a stronger correlation. In the case of commercial ZnO samples, the r^2 value was 0.1163, indicating a limited agreement. Conversely, the commercial ZnO/BC nanocomposites exhibited a higher r^2 value of 0.8399, indicating a robust correlation. For the prepared ZnO samples, an r^2 value of 0.9429 was attained, demonstrating a highly significant correspondence. Similarly, the prepared ZnO/BC nanocomposites showed a notable r^2 value of 0.9232, indicating a relatively strong relationship. These r^2 values provide valuable insights into the alignment between the second-order kinetic model and the experimental data for the different materials and their composites.

Our experimental investigation on the degradation behaviour of methyl orange, using ZnO and TiO_2 nanoparticles, as well as their composite, reveals that the degradation rate follows a first-order kinetic model. In contrast, the second-order kinetic model, which was also evaluated in our study, showed lower correlation coefficient, and inconsistency as shown in table 4.2. This further supports our conclusion that the degradation of methyl orange in our experimental conditions is best described by a first-order kinetic model.

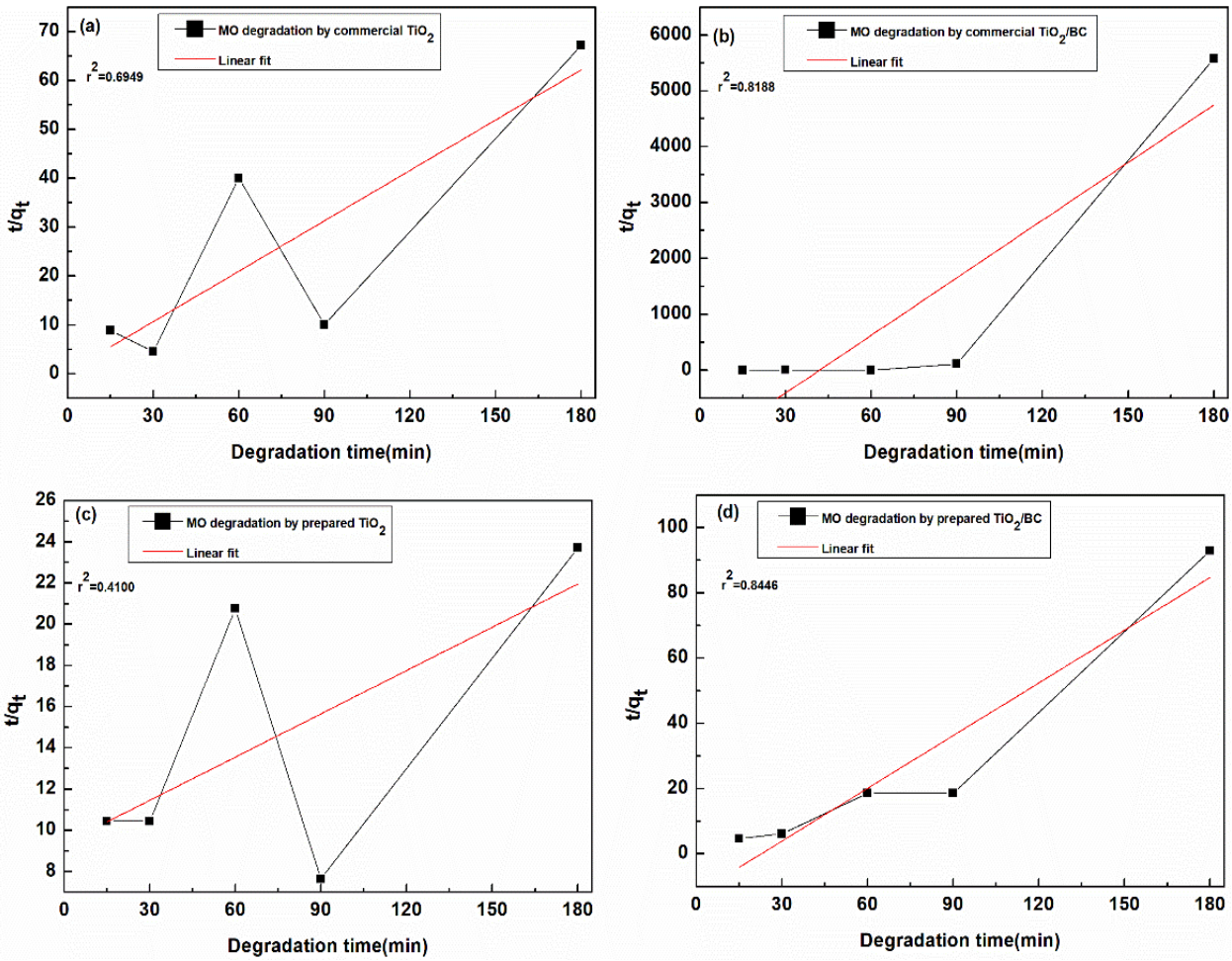

Figure 4.30:Second order kinetic analysis of MO under (a) commercial TiO_2, (b) commercial TiO_2 /BC, (c) prepared TiO_2 and (d) prepared TiO_2/ BC.

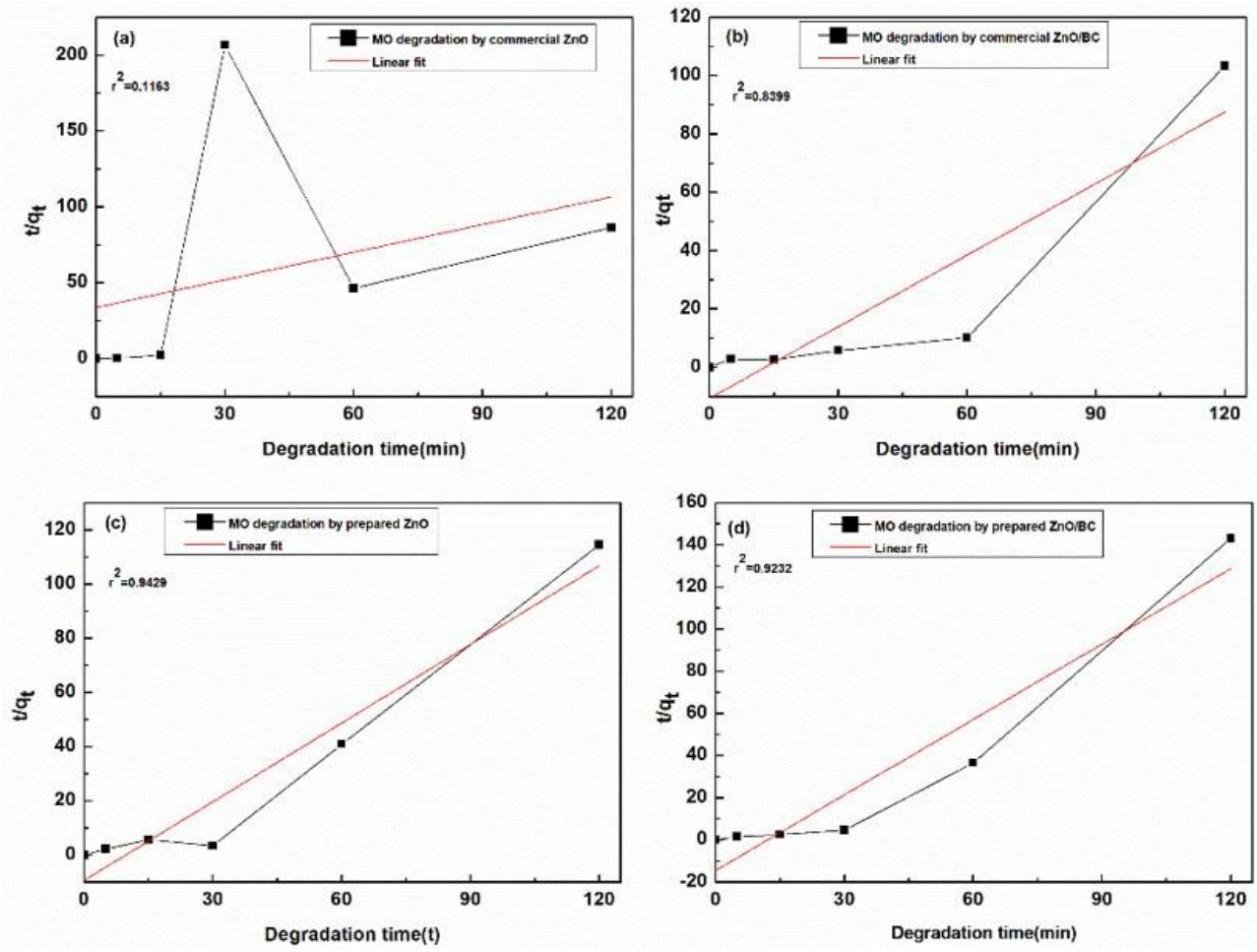

Figure 4.31:Second order kinetic analysis of MO under (a) commercial ZnO, (b) commercial ZnO /BC, (c) prepared ZnO and (d) prepared ZnO /BC.

Table 4.2:Kinetic parameters for second order kinetic model of MO

Catalyst	q_e (mg/g)	K(g/mg^{-1}min^{-1})	r^2
Commercial TiO_2	2.911	0.3026	0.6949
Commercial TiO_2 BC	0.02912	-0.8246	0.8188
Prepared TiO_2	13.85	0.0005385	0.4100
Prepared TiO_2 BC	1.586	-0.02600	0.8446
Commercial ZnO	1.645	0.01094	0.1163
Commercial ZnO BC	1.223	-0.06370	0.8399
Prepared ZnO	1.034	-0.1007	0.9429
Prepared ZnO BC	0.8403	-0.09830	0.9232

5 Conclusion

This study provides valuable insights into the photocatalytic decolorisation of methyl orange using catalysts, including TiO_2, ZnO nanoparticles, and their composites with biochar. Following conclusion can be drawn from this study.

- Novel TiO_2 or ZnO along with TiO_2 and ZnO based biochar composites were successfully prepared by the Autoclave method. This preparation technique presents a promising field for the development of advanced catalyst materials.

- Photocatalytic decolorization of methyl orange was investigated using various catalysts, including TiO_2, ZnO nanoparticles, and their composites with biochar (BC). Furthermore, the study compared the efficacy of produced TiO_2 catalysts to commercial TiO_2 catalysts when deteriorating MO. Prepared TiO_2 catalysts exceed the commercial in degrading methyl orange, demonstrating superior photocatalytic activity. Moreover, SDS, in the prepared TiO_2 composition plays a crucial role in its effectiveness and reducing degree of agglomeration of TiO_2 nano particles. Similarly, photocatalytic activity of prepared ZnO was found better than commercial ZnO.

- More than 90 percent degradation was observed in the presence of biochar containing TiO_2 or ZnO nanoparticles in this study. By narrowing the band gap and expanding the range of light absorption, biochar enhances the interaction between organic matter and the catalyst, which improves the utilization of electrons generated by photocatalysis, and ultimately improves the overall photocatalytic performance of TiO_2 and ZnO catalysts. Consequently, the photocatalytic activity of the biochar-containing composites was improved. Using a wider spectrum of light, these catalysts can degrade methyl orange more efficiently, leading to their amazing degradation properties.

- The SEM-EDS data indicated that TiO_2 and ZnO nanoparticles were uniformly dispersed on the surface of biochar and the presence of all components was confirmed by the element distribution analysis.

- XRD patterns revealed that all prepared composites are presented in crystalline form.

- The study found that an adsorption ratio of 1:1 between the catalyst and methyl orange solution, with a dye concentration of 75 mg in 75 ml of methyl orange stock solution whose concentration is 20 ppm (20 mg/L), resulted in the maximum decolorisation rate. While the study did not investigate other adsorption ratios, the identified optimal ratio can serve as an important tool for future research on the photocatalytic degradation of methyl orange and other organic pollutants.

- Furthermore, our analysis indicates that the pseudo first order kinetic model best describes the kinetics of the decolorisation process, as demonstrated by the notably high correlation coefficient value. However, the experimental data did not fit well with the pseudo-seond order model, indicating the need for further investigation into the mechanism underlying the photocatalytic degradation of methyl orange. These findings have important implications for the development of effective strategies for water treatment and environmental remediation.

- The experimental data demonstrated that TiO_2, ZnO and biochar composites could be promising photocatalysts suitable for aqueous environment remediation.

6 Future Work

Although the study found that the pseudo first-order kinetic model best describes the kinetics of the decolorization process, the experimental data did not fit well with the pseudo second - order kinetic model. Therefore, further investigation is needed to better understand the underlying mechanism of the photocatalytic degradation process. While methyl orange was used as the model dye in this study, there are a variety of dyes, such as methylene blue and Congo Red, as well as antibiotics, such as paracetamol and diclofenac [71], that could be photocatalytically degraded using the catalysts investigated in this study. Future research could investigate the effectiveness of catalysts in degrading these contaminants.

References

[1] K. Abbass, M. Z. Qasim, H. Song, M. Murshed, H. Mahmood, and I. Younis, 'A review of the global climate change impacts, adaptation, and sustainable mitigation measures', *Environ. Sci. Pollut. Res.*, vol. 29, no. 28, pp. 42539–42559, Jun. 2022, doi: 10.1007/s11356-022-19718-6.

[2] L. Wu *et al.*, 'Study on the adsorption properties of methyl orange by natural one-dimensional nano-mineral materials with different structures', *Sci. Rep.*, vol. 11, no. 1, p. 10640, May 2021, doi: 10.1038/s41598-021-90235-1.

[3] N. A. Ramos-Delgado, M. Á. Gracia-Pinilla, R. V. Mangalaraja, K. O'Shea, and D. D. Dionysiou, 'Industrial synthesis and characterization of nanophotocatalysts materials: titania', *Nanotechnol. Rev.*, vol. 5, no. 5, Jan. 2016, doi: 10.1515/ntrev-2016-0007.

[4] J. Gómez-Pastora, S. Dominguez, E. Bringas, M. J. Rivero, I. Ortiz, and D. D. Dionysiou, 'Review and perspectives on the use of magnetic nanophotocatalysts (MNPCs) in water treatment', *Chem. Eng. J.*, vol. 310, pp. 407–427, Feb. 2017, doi: 10.1016/j.cej.2016.04.140.

[5] A. Fujishima and K. Honda, 'Electrochemical Photolysis of Water at a Semiconductor Electrode', *Nature*, vol. 238, no. 5358, pp. 37–38, Jul. 1972, doi: 10.1038/238037a0.

[6] J. Zhuang *et al.*, 'Photocatalytic Degradation of RhB over TiO_2 Bilayer Films: Effect of Defects and Their Location', *Langmuir*, vol. 26, no. 12, pp. 9686–9694, Jun. 2010, doi: 10.1021/la100302m.

[7] I. Dolamic and T. Bürgi, 'In Situ ATR-IR Study on the Photocatalytic Decomposition of Amino Acids over Au/TiO_2 and TiO_2', *J. Phys. Chem. C*, vol. 115, no. 5, pp. 2228–2234, Feb. 2011, doi: 10.1021/jp1102753.

[8] H. Dong *et al.*, 'An overview on limitations of TiO_2-based particles for photocatalytic degradation of organic pollutants and the corresponding countermeasures', *Water Res.*, vol. 79, pp. 128–146, Aug. 2015, doi: 10.1016/j.watres.2015.04.038.

[9] V. Etacheri, C. Di Valentin, J. Schneider, D. Bahnemann, and S. C. Pillai, 'Visible-light activation of TiO2 photocatalysts: Advances in theory and experiments', *J. Photochem. Photobiol. C Photochem. Rev.*, vol. 25, pp. 1–29, Dec. 2015, doi: 10.1016/j.jphotochemrev.2015.08.003.

[10] R. Asahi, T. Morikawa, T. Ohwaki, K. Aoki, and Y. Taga, 'Visible-Light Photocatalysis in Nitrogen-Doped Titanium Oxides', *Sci. New Ser.*, vol. 293, no. 5528, pp. 269–271, 2001.

[11] S. U. M. Khan, M. Al-Shahry, and W. B. Ingler, 'Efficient Photochemical Water Splitting by a Chemically Modified n-TiO_2', *Science*, vol. 297, no. 5590, pp. 2243–2245, Sep. 2002, doi: 10.1126/science.1075035.

[12] L. Li *et al.*, 'Hydrothermal synthesis and gas sensing properties of single-crystalline ultralong ZnO nanowires', *Appl. Phys. A*, vol. 98, no. 3, pp. 635–641, Mar. 2010, doi: 10.1007/s00339-009-5457-y.

[13] X. Wang, J. Zhou, J. Song, J. Liu, N. Xu, and Z. L. Wang, 'Piezoelectric Field Effect Transistor and Nanoforce Sensor Based on a Single ZnO Nanowire', *Nano Lett.*, vol. 6, no. 12, pp. 2768–2772, Dec. 2006, doi: 10.1021/nl061802g.

[14] S. Chu *et al.*, 'Electrically pumped waveguide lasing from ZnO nanowires', *Nat. Nanotechnol.*, vol. 6, no. 8, pp. 506–510, Aug. 2011, doi: 10.1038/nnano.2011.97.

[15] X.-M. Zhang, M.-Y. Lu, Y. Zhang, L.-J. Chen, and Z. L. Wang, 'Fabrication of a High-Brightness Blue-Light-Emitting Diode Using a ZnO-Nanowire Array Grown on p-GaN Thin

Film', *Adv. Mater.*, vol. 21, no. 27, pp. 2767–2770, Jul. 2009, doi: 10.1002/adma.200802686.
[16] C. M. Firdaus, M. S. B. S. Rizam, M. Rusop, and S. R. Hidayah, 'Characterization of ZnO and ZnO: TiO2 Thin Films Prepared by Sol-Gel Spray-Spin Coating Technique', *Procedia Eng.*, vol. 41, pp. 1367–1373, 2012, doi: 10.1016/j.proeng.2012.07.323.
[17] L. Lu, R. Shan, Y. Shi, S. Wang, and H. Yuan, 'A novel TiO2/biochar composite catalysts for photocatalytic degradation of methyl orange', *Chemosphere*, vol. 222, pp. 391–398, May 2019, doi: 10.1016/j.chemosphere.2019.01.132.
[18] M. G. Gonçalves, P. A. Da Silva Veiga, M. R. Fornari, P. Peralta-Zamora, A. S. Mangrich, and S. Silvestri, 'Relationship of the physicochemical properties of novel ZnO/biochar composites to their efficiencies in the degradation of sulfamethoxazole and methyl orange', *Sci. Total Environ.*, vol. 748, p. 141381, Dec. 2020, doi: 10.1016/j.scitotenv.2020.141381.
[19] J.-M. Herrmann, 'Heterogeneous photocatalysis: fundamentals and applications to the removal of various types of aqueous pollutants', *Catal. Today*, vol. 53, no. 1, pp. 115–129, Oct. 1999, doi: 10.1016/S0920-5861(99)00107-8.
[20] D. D. Thongam and H. Chaturvedi, 'Advances in nanomaterials for heterogeneous photocatalysis', *Nano Express*, vol. 2, no. 1, p. 012005, Mar. 2021, doi: 10.1088/2632-959X/abeb8d.
[21] N. Daneshvar, D. Salari, and A. R. Khataee, 'Photocatalytic degradation of azo dye acid red 14 in water on ZnO as an alternative catalyst to TiO_2', *J. Photochem. Photobiol. Chem.*, vol. 162, no. 2–3, pp. 317–322, Mar. 2004, doi: 10.1016/S1010-6030(03)00378-2.
[22] D. Zhu and Q. Zhou, 'Action and mechanism of semiconductor photocatalysis on degradation of organic pollutants in water treatment: A review', *Environ. Nanotechnol. Monit. Manag.*, vol. 12, p. 100255, Dec. 2019, doi: 10.1016/j.enmm.2019.100255.
[23] Y. Zhang, M. K. Ram, E. K. Stefanakos, and D. Y. Goswami, 'Synthesis, Characterization, and Applications of ZnO Nanowires', *J. Nanomater.*, vol. 2012, pp. 1–22, 2012, doi: 10.1155/2012/624520.
[24] L. K. Krasteva, K. I. Papazova, A. S. Bojinova, N. V. Kaneva, and A. A. Apostolov, 'Synthesis and characterization of ZnO and TiO_2 powders, nanowire ZnO and TiO2/ZnO thin films for photocatalyc applications'.
[25] A. Ibhadon and P. Fitzpatrick, 'Heterogeneous Photocatalysis: Recent Advances and Applications', *Catalysts*, vol. 3, no. 1, pp. 189–218, Mar. 2013, doi: 10.3390/catal3010189.
[26] D. S. Bhatkhande, V. G. Pangarkar, and A. A. Beenackers, 'Photocatalytic degradation for environmental applications - a review', *J. Chem. Technol. Biotechnol.*, vol. 77, no. 1, pp. 102–116, Jan. 2002, doi: 10.1002/jctb.532.
[27] K. Pirkanniemi and M. Sillanpää, 'Heterogeneous water phase catalysis as an environmental application: a review', *Chemosphere*, vol. 48, no. 10, pp. 1047–1060, Sep. 2002, doi: 10.1016/S0045-6535(02)00168-6.
[28] Y. I. Matatov-Meytal and M. Sheintuch, 'Catalytic Abatement of Water Pollutants', *Ind. Eng. Chem. Res.*, vol. 37, no. 2, pp. 309–326, Feb. 1998, doi: 10.1021/ie9702439.
[29] D. Chen *et al.*, 'Photocatalytic degradation of organic pollutants using TiO2-based photocatalysts: A review', *J. Clean. Prod.*, vol. 268, p. 121725, Sep. 2020, doi: 10.1016/j.jclepro.2020.121725.
[30] R. C. Bhave and B. I. Lee, 'Experimental variables in the synthesis of brookite phase TiO2 nanoparticles', *Mater. Sci. Eng. A*, vol. 467, no. 1–2, pp. 146–149, Oct. 2007, doi: 10.1016/j.msea.2007.02.092.

[31] A. H. Navidpour, S. Abbasi, D. Li, A. Mojiri, and J. L. Zhou, 'Investigation of Advanced Oxidation Process in the Presence of TiO2 Semiconductor as Photocatalyst: Property, Principle, Kinetic Analysis, and Photocatalytic Activity', *Catalysts*, vol. 13, no. 2, p. 232, Jan. 2023, doi: 10.3390/catal13020232.
[32] L. Cao, D. Chen, W.-Q. Wu, J. Z. Y. Tan, and R. A. Caruso, 'Monodisperse anatase titania microspheres with high-thermal stability and large pore size (∼80 nm) as efficient photocatalysts', *J. Mater. Chem. A*, vol. 5, no. 7, pp. 3645–3654, 2017, doi: 10.1039/C6TA08981J.
[33] J. Zhang, P. Zhou, J. Liu, and J. Yu, 'New understanding of the difference of photocatalytic activity among anatase, rutile and brookite TiO_2', *Phys. Chem. Chem. Phys.*, vol. 16, no. 38, pp. 20382–20386, 2014, doi: 10.1039/C4CP02201G.
[34] X. Yan and X. Chen, 'Titanium Dioxide Nanomaterials', in *Encyclopedia of Inorganic and Bioinorganic Chemistry*, R. A. Scott, Ed., Chichester, UK: John Wiley & Sons, Ltd, 2015, pp. 1–38. doi: 10.1002/9781119951438.eibc2335.
[35] A. Hernández Battez et al., 'CuO, ZrO2 and ZnO nanoparticles as antiwear additive in oil lubricants', Wear, vol. 265, no. 3–4, pp. 422–428, Jul. 2008, doi: 10.1016/j.wear.2007.11.013.
[36] M. K. Sikdar, G. Ghorai, T. R. Senapati, and P. K. Sahoo, 'Modulation of bandgap and electrical conductivity in europium doped single ZnO nanorod device', *J. Alloys Compd.*, vol. 913, p. 165179, Aug. 2022, doi: 10.1016/j.jallcom.2022.165179.
[37] C. X. Xu, X. W. Sun, Z. L. Dong, G. P. Zhu, and Y. P. Cui, 'Zinc oxide hexagram whiskers', *Appl Phys Lett*, 2014.
[38] S. Iwan, V. Fauzia, A. A. Umar, and X. W. Sun, 'Room temperature photoluminescence properties of ZnO nanorods grown by hydrothermal reaction', presented at the INTERNATIONAL SYMPOSIUM ON CURRENT PROGRESS IN MATHEMATICS AND SCIENCES 2015 (ISCPMS 2015): Proceedings of the 1st International Symposium on Current Progress in Mathematics and Sciences, Depok, Indonesia, 2016, p. 020031. doi: 10.1063/1.4946934.
[39] Z. L. Wang, 'Zinc oxide nanostructures: growth, properties and applications', *J. Phys. Condens. Matter*, vol. 16, no. 25, pp. R829–R858, Jun. 2004, doi: 10.1088/0953-8984/16/25/R01.
[40] J. Wojnarowicz, T. Chudoba, and W. Lojkowski, 'A Review of Microwave Synthesis of Zinc Oxide Nanomaterials: Reactants, Process Parameters and Morphologies', *Nanomaterials*, vol. 10, no. 6, p. 1086, May 2020, doi: 10.3390/nano10061086.
[41] M. Mehrabian, R. Azimirad, K. Mirabbaszadeh, H. Afarideh, and M. Davoudian, 'UV detecting properties of hydrothermal synthesized ZnO nanorods', *Phys. E Low-Dimens. Syst. Nanostructures*, vol. 43, no. 6, pp. 1141–1145, Apr. 2011, doi: 10.1016/j.physe.2011.01.030.
[42] N. Joudeh and D. Linke, 'Nanoparticle classification, physicochemical properties, characterization, and applications: a comprehensive review for biologists', *J. Nanobiotechnology*, vol. 20, no. 1, p. 262, Jun. 2022, doi: 10.1186/s12951-022-01477-8.
[43] M. A. Shaheed and F. H. Hussein, 'Preparation and Applications of Titanium Dioxide and Zinc Oxide Nanoparticles', *J. Environ. Anal. Chem.*, vol. 02, no. 01, 2014, doi: 10.4172/JREAC.1000e109.
[44] R. A. Gonçalves, R. P. Toledo, N. Joshi, and O. M. Berengue, 'Green Synthesis and Applications of ZnO and TiO2 Nanostructures', *Molecules*, vol. 26, no. 8, p. 2236, Apr. 2021, doi: 10.3390/molecules26082236.

[45] B. P. Kafle, "Chemical Analysis and Material Characterization by Spectrophotometry," Elsevier, 2019.
[46] H. Hayashi and Y. Hakuta, 'Hydrothermal Synthesis of Metal Oxide Nanoparticles in Supercritical Water', *Materials*, vol. 3, no. 7, pp. 3794–3817, Jun. 2010, doi: 10.3390/ma3073794.
[47] E. Gabano and M. Ravera, 'Microwave-Assisted Synthesis: Can Transition Metal Complexes Take Advantage of This "Green" Method?', *Molecules*, vol. 27, no. 13, p. 4249, Jun. 2022, doi: 10.3390/molecules27134249.
[48] N. A. Yazid and Y. C. Joon, 'Co-precipitation synthesis of magnetic nanoparticles for efficient removal of heavy metal from synthetic wastewater', presented at the 6TH INTERNATIONAL CONFERENCE ON ENVIRONMENT (ICENV2018): Empowering Environment and Sustainable Engineering Nexus Through Green Technology, Penang, Malaysia, 2019, p. 020019. doi: 10.1063/1.5117079.
[49] N. T. K. Thanh, N. Maclean, and S. Mahiddine, 'Mechanisms of Nucleation and Growth of Nanoparticles in Solution', *Chem. Rev.*, vol. 114, no. 15, pp. 7610–7630, Aug. 2014, doi: 10.1021/cr400544s.
[50] A. T. Odularu, 'Metal Nanoparticles: Thermal Decomposition, Biomedicinal Applications to Cancer Treatment, and Future Perspectives', *Bioinorg. Chem. Appl.*, vol. 2018, pp. 1–6, 2018, doi: 10.1155/2018/9354708.
[51] Q.-Q. Qiu, W.-Q. Sun, and J. Connor, 'Sterilization of Biomaterials of Synthetic and Biological Origin', in *Comprehensive Biomaterials*, Elsevier, 2011, pp. 127–144. doi: 10.1016/B978-0-08-055294-1.00248-8.
[52] D. M. Mattox, *Handbook of physical vapor deposition (PVD) processing*, 2nd ed. Oxford, UK: William Andrew, 2010.
[53] A. Vahl *et al.*, 'Pathways to Tailor Photocatalytic Performance of TiO_2 Thin Films Deposited by Reactive Magnetron Sputtering', *Materials*, vol. 12, no. 17, p. 2840, Sep. 2019, doi: 10.3390/ma12172840.
[54] H. O. Pierson and H. O. Pierson, *Handbook of chemical vapor deposition*, 2nd ed. Norwich, NY: Noyes Publications, 1999.
[55] O. Lupan *et al.*, 'Synthesis and characterization of ZnO nanowires for nanosensor applications', *Mater. Res. Bull.*, vol. 45, no. 8, pp. 1026–1032, Aug. 2010, doi: 10.1016/j.materresbull.2010.03.027.
[56] H. Liu, Y. Zhang, R. Li, M. Cai, and X. Sun, 'Synthesis and characterization of TiO2@C core-shell nanowires and nanowalls via chemical vapor deposition for potential large-scale production', *J. Colloid Interface Sci.*, vol. 367, no. 1, pp. 115–119, Feb. 2012, doi: 10.1016/j.jcis.2011.09.022.
[57] D. Bokov *et al.*, 'Nanomaterial by Sol-Gel Method: Synthesis and Application', *Adv. Mater. Sci. Eng.*, vol. 2021, pp. 1–21, Dec. 2021, doi: 10.1155/2021/5102014.
[58] T. M. Albayati, G. M. Alwan, and O. S. Mahdy, 'High performance methyl orange capture on magnetic nanoporous MCM-41 prepared by incipient wetness impregnation method', *Korean J. Chem. Eng.*, vol. 34, no. 1, pp. 259–265, Jan. 2017, doi: 10.1007/s11814-016-0231-2.
[59] M. F. Hadi Al-kadhemy, A. AbdulMunem Saeed, F. J. Kadhum, S. A. Mazloum, and H. K. Aied, 'The effect of (He–Ne) laser irradiation on the optical properties of methyl orange doped PVA films', *J. Radiat. Res. Appl. Sci.*, vol. 7, no. 3, pp. 371–375, Jul. 2014, doi: 10.1016/j.jrras.2014.05.006.

[60] K. Obaideen, N. Shehata, E. T. Sayed, M. A. Abdelkareem, M. S. Mahmoud, and A. G. Olabi, 'The role of wastewater treatment in achieving sustainable development goals (SDGs) and sustainability guideline', *Energy Nexus*, vol. 7, p. 100112, Sep. 2022, doi: 10.1016/j.nexus.2022.100112.

[61] Y. Idrees, "Microstructural Evolution in Zr and Zr Alloy Excel under Ion Irradiation," Ph.D. thesis, Department of Mechanical and Materials Engineering, Queen's University, Kingston, Ontario, Canada, December 2013.

[62] L. Ernawati *et al.*, 'Kinetic Studies of Methylene Blue Degradation using $CaTiO_3$ Photocatalyst from Chicken Eggshells', *J. Phys. Conf. Ser.*, vol. 1726, no. 1, p. 012017, Jan. 2021, doi: 10.1088/1742-6596/1726/1/012017.

[63] E. D. Revellame, D. L. Fortela, W. Sharp, R. Hernandez, and M. E. Zappi, 'Adsorption kinetic modeling using pseudo-first order and pseudo-second order rate laws: A review', *Clean. Eng. Technol.*, vol. 1, p. 100032, Dec. 2020, doi: 10.1016/j.clet.2020.100032.

[64] I. Oshina and J. Spigulis, 'Beer–Lambert law for optical tissue diagnostics: current state of the art and the main limitations', *J. Biomed. Opt.*, vol. 26, no. 10, Oct. 2021, doi: 10.1117/1.JBO.26.10.100901.

[65] M. Verma, K. B. Sharma, and N. S. Saxena, 'Enhanced photodegradation of methylene blue by silica coated ZnSe nanoparticles', *INDIAN J PURE APPL PHYS*, vol. 57, 2019.

[66] K. Thamaphat, P. Limsuwan, and B. Ngotawornchai, 'Phase Characterization of TiO2 Powder by XRD and TEM'.

[67] W. Li, R. Liang, A. Hu, Z. Huang, and Y. N. Zhou, 'Generation of oxygen vacancies in visible light activated one-dimensional iodine TiO_2 photocatalysts', *RSC Adv*, vol. 4, no. 70, pp. 36959–36966, 2014, doi: 10.1039/C4RA04768K.

[68] M. Achehboune, M. Khenfouch, I. Boukhoubza, B. Mothudi, I. Zorkani, and A. Jorio, 'Study on the effect of Er dopant on the structural properties of ZnO nanorods synthesized via hydrothermal method', *J. Phys. Conf. Ser.*, vol. 1292, no. 1, p. 012020, Aug. 2019, doi: 10.1088/1742-6596/1292/1/012020.

[69] Y. Liu, M. Paskevicius, M. V. Sofianos, G. Parkinson, S. Wang, and C.-Z. Li, 'A SAXS study of the pore structure evolution in biochar during gasification in H2O, CO2 and H2O/CO2', *Fuel*, vol. 292, p. 120384, May 2021, doi: 10.1016/j.fuel.2021.120384.

[70] N. P. F. Gonçalves, M. A. O. Lourenço, S. R. Baleuri, S. Bianco, P. Jagdale, and P. Calza, 'Biochar waste-based ZnO materials as highly efficient photocatalysts for water treatment', *J. Environ. Chem. Eng.*, vol. 10, no. 2, p. 107256, Apr. 2022, doi: 10.1016/j.jece.2022.107256.

[71] J. Żur, A. Piński, D. Wojcieszyńska, W. Smułek, and U. Guzik, 'Diclofenac Degradation—Enzymes, Genetic Background and Cellular Alterations Triggered in Diclofenac-Metabolizing Strain Pseudomonas moorei KB4', *Int. J. Mol. Sci.*, vol. 21, no. 18, p. 6786, Sep. 2020, doi: 10.3390/ijms21186786.

List of Figures

List of Tables

Appendix

Appendix I- List of Symbols

ev	electron-volt
mg	Milligram
L	Litre
E	Energy
h	Planck constant
v	Frequency of incident light
e-	Electron
h+	Hole
$OH\cdot$	Hydroxyl radical
O_2^-	Superoxide radical
H_2O_2	peroxides
O_2	Oxygen
CdS	Cadmium sulfide
$SrTiO_3$	Strontium titanate
WSe_2	Tungsten diselenide
α-Fe_2O_3	Alpha-phase iron (III) oxide
Fe_2O_3	Ferric oxide
WO_3	Tungsten trioxode
ZnS	Zinc sulfide
SnO_2	Tin oxide
Si	Silicon
Ru	Ruthenium
Pt	Platinium
Rh	Rhodium
Ir	Iridium
Pd	Palladium
Cu	Copper
Mn	Manganese

Co	Cobalt
Cr	Chromium
Ti	Titanium
Bi	Bismuth
Zn	Zinc
A^o	Angstorm
S cm^{-1}	Siemens per centimeter
V	Vanadium
pH	Power of hydroen
C	Carbon
ppm	Parts per million, mg/L
g	Gram
λ	Wavelength
mA	Milliampere
n	Integer
θ	Angle
d	interplanar spacing or distance
nm	Nanometers
q_t	Amount of methyl orange adsorbed at time (mg g^{-1})
qe	Amount of methyl orange adsorbed at the equilibrium (mg g-1)
K	Pseudo second order rate constant (g mg-1 min-1)
Vs	Volume of solution (L)
W	Amount of catalyst dose (gL^{-1})
C_0	Initial dye concentrations (mg L^{-1})
C_e	Equilibrium dye concentrations (mg L^{-1})
C_t	Instantaneous dye concentrations (mg L^{-1})
A	Absorbance (a.u)
ε	Molar absorptivity (L $mol^{-1}cm^{-1}$)
b	Path length (cm)
k	Pseudo first order rate constant(min^{-1})
Al	Aluminium
Zn^{2+}	Zinc ion

M	Molarity

Appendix II- List of Acronyms and Nomenclature

TiO_2	Titanium dioxide
ZnO	Zinc oxide
H_2O	Water
CO_2	Carbon dioxide
SEM	Scanning Electron Microscopy
EDS	Energy Dispersive Spectroscopy
XRD	X-ray Diffraction
FTIR	Fourier transform infrared
RhB	Rhodamine B
SMX	Sulfamethoxazole
UV	Ultraviolet
ZnOMBNC	Zinc oxide Modified Biochar Nanocomposites
VB	Valence band
CB	Conduction band
$C_{14}H_{14}N_3SO_3Na$	Methyl Orange
C_2H_5OH	Ethanol
$C_{16}H_{36}O_4Ti$	Titanium (IV) butoxide
$Zn(CH_3COO)_2 \cdot 2H_2O$	Zinc acetate dehydrate
NaOH	Sodium hydroxide
SDS	Sodium dodecyl sulfate
MO	Methyl Orange
RI	Refractive index

Appendix III- Images of some sample

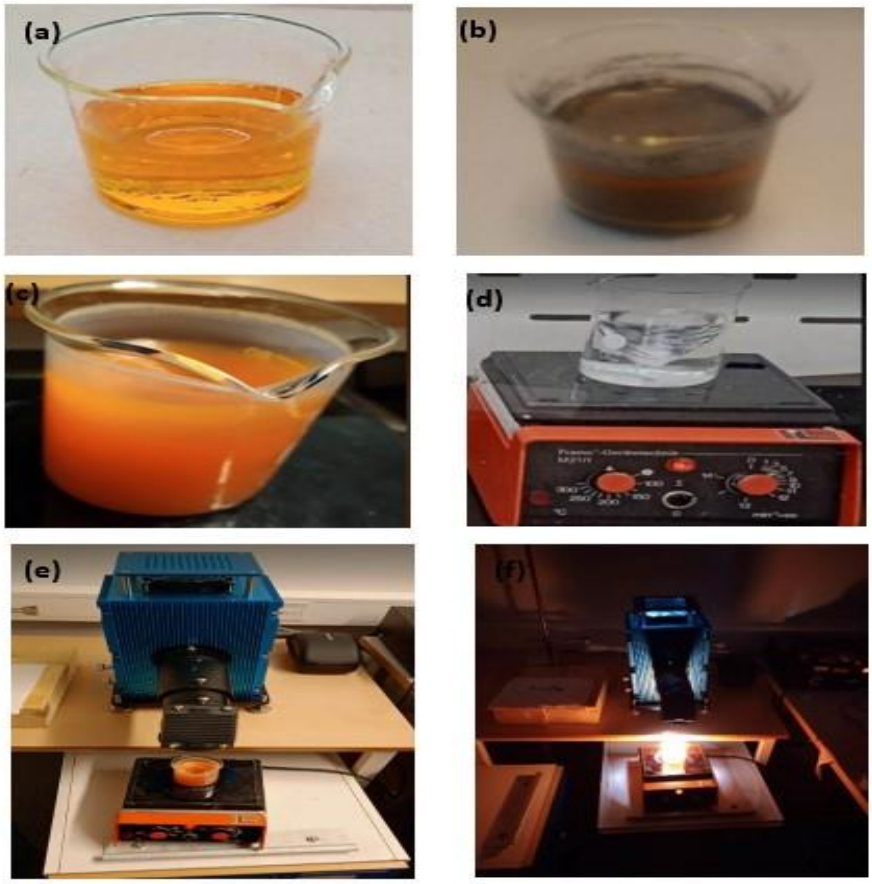

Figure 6.1: Sample representing (a) pure MO solution, (b) MO and BC solution, (c) prepared ZnO and MO before solar and (d) prepared ZnO and MO after 150 min solar, (e) prepared TiO_2 and MO solution before solar and (f) prepared TiO_2 and MO solution after240 min of solar.